NTNU
Norwegian University of
Science and Technology

DFT studies of BaTiO3 interfaces

Sindre Tuset

Master of Science in Electronics
Submission date: July 2016
Supervisor: Thomas Tybell, IET
Co-supervisor: Magnus Moreau, IET

Norwegian University of Science and Technology
Department of Electronics and Telecommunications

Problem formulation

Recent studies have shown that interfaces between different oxides can show new electronic and magnetic properties. These nanostructures and interface engineering has many potential applications and is a large area of research internationally.

Density functional theory (DFT) calculations is a useful tool in this respect. DFT is a quantum mechanical method to solve the many-body Schrödinger equation numerically, and allows the derivation of properties like ferroelectric polarization, structure, magnetic properties etc. on length scales that can be difficult to achieve experimentally. This makes DFT an appropriate tool to examine functional interfaces. In this master thesis will examine thin slabs of BaTiO3, with particular interest in studying how the crystallographic direction of the interface affects ferroelectric polarization and order parameter.

Thomas Tybell

Abstract

This thesis has explored some of the nuances of Density Funtional Theory, ferroelectricity and oxide perovskites, $BaTiO_3$ in particular. The effects of strain and crystal orientation on phase diagram and polarization in BTO has been investigated using DFT calculations and Berry phase analysis. There has been done DFT calculations on bulk BTO as well as epitaxially strained BTO, and by using Berry phase analysis the polarization magnitude and direction of the structures have been estimated.
The polarization of (001) strained BTO increase for both compressive and tensile strain as the favoured structure transition from a P4mm symmetry with the extraordinary axis out of the strain plane via a Cm symmetry to a Amm2 symmetry with ion displacements along the pseudocubic [110] direction. For the (111) strained samples the structure has a first order phase transition at 1.5% tensile strain from a Cm symmetry with ion displacements in the out of plane [111] direction to a P1 symmetry. The results from the tetragonal phase is used to get an estimate of the behaviour at room temperature, as the tetragonal phase is favoured between 5°C and 120°C. This shows similar results as for the rhombohedral phase for (111) strained samples. The work done in this thesis lays the theoretical groundwork for a polar phase for compressive strain in (111) strained BTO, where all the polar phases converge to a polar out of plane phase for compressive strain using the PBEsol functional [1, 2]. This is contrary to some of the previous work done on (111) oriented BTO stating that BTO relaxes to a non-polar R-3m symmetry for compressive strain values [3, 4] where the LDA functional [5] has been used.

Preface

> Err and err and err again, but less and less and less.
>
> Piet Hein

The work detailed in this report has been carried out at the Department of Electronics and Telecommunications at NTNU during the spring semester of 2016, and serves as the masters thesis in the M.Tech. program in Electronics. My work has also been supported in part by the Materials Simulation Center, a Penn-State MRSEC and MRI facility. Parts of my work was performed on the Abel Cluster, owned by the University of Oslo and the Norwegian metacenter for High Performance Computing (NOTUR), and operated by the Department for Research Computing at USIT, the University of Oslo IT-department. The work done on Abel has been supported by the Research Council of Norway.

Acknowledgements

A special thanks is given to my ever-enthusiastic supervisor professor Thomas Tybell. His guidance and leadership has proven very helpful during the work on this thesis. I would also like to extend my sincerest gratitude to M.Sc. Magnus Moreau. He has been a tremendous help to me with technical issues, healthy discussions and theoretical guidance. Their collective help and input has been invaluable. Furthermore I would like to acknowledge with great appreciation the contributions from the Oxide Electronics Lab at the Department of Electronics and Telecommunications. Additional acknowledgements is also given to the VASP technical group, coordinated by Sverre Magnus Selbach, for being a place of collegiality and shared excitement and frustration. Finally my thanks go to my parents, my brother and my sister, to whom my gratitude has no limits.
Sindre Tuset
Trondheim, July 2016

Contents

List of Figures

List of Tables

Chapter 1

Introduction

This chapter seeks to lay a foundation of the state of the art in the field of ferroelectrics, with special focus on perovskite oxides, strain effects on the ferroelectric properties of ferroelectrics and the significance of strain directionality.

1.1 State of the art

Ferroelectrics

Ferroelectrics are considered good candidates for being promising materials for many applications, such as memory[6], transistors [7], photovoltaics [8], capacitors[9], multiferroicity and magnetoelectric coupling [10–12], colossal magnetoresistance [13] etc. $BaTiO_3$ (BTO) is one of the most studied and interesting perovskite ferroelectrics to date [14] and it has stayed interesting due to developements in maintaining hte ferroelectric response even for ultra-thin films[15]. The applications of BTO in heterostructures with other materials is also being studied. Ferroelectric BTO has been shown to manipulate the orbital occupation of electrons in $LaNiO_3$, opening for the possibility of electrical control of orbital polarization at an oxide interface [16].

Strain vs. Polarization

Seeing as all ferroelectrics are piezoelectric, the coupling between strain and polarization is imminent. The coupling was known as one of the discrepancies between the ferroelectric and ferromagnetic effects from the onset, as magnetoelastic coefficients are generally measured in parts per million, whereas the electroelastic coupling is in the order of percent [17]. Especially for thin film applications, the strain-polarization curve is important, as thin films are subjected to the strain of the substrate or crystal it is grown on. For compressive (001) strain values, the out of plane polarization mode for tetragonal BTO is made stable on a series of substrates and bilayer structures, among others $La_{0.7}Sr_{0.3}MnO_3$ [18]. A group published a study in 2008 doing (111) strain calculations on both BTO and $PbTiO_3$, showing a strain dependence on the phases of both materials for strain values between -1.5% and 1.5% done with DFT calculations. A similar calculations were done by Raeliarijaona and Fu [3], showing the strain dependence of the polarization in (111) strained BTO.

(001) vs (111)

The orientation of a crystal structure submitted to strain has been shown to have great effect on the physical properties of the material. Li et.al [19] showed that the orientation of $BiFeO_3$ greatly effected the phase diagram and the ferroelectric polarization. In 2013, the effect of epitaxial orientation with respect to piezoelectric properties in lead-free $0.5BaZr0.2Ti0.8O_3$-$0.5Ba0.7Ca0.3TiO_3$ was explored, showing a piezoelectric response in (111) strained crystals similar to that of (001) strained crystals. The study considered (001), (011) and (111) strained samples, focusing on the change in piezoelectric coefficient as a function of orientation and strain [20]. More recently, Wu et.al. [21] did similar studies on BTO films using an expanded nonlinear thermodynamic theory model. The BTO was shown to have more complicated phase transitions for (011)-oriented films, increasing the Curie temperature dramatically for compressive strain. A study from 2014 [3] suggested that the theoretical ferroelectric response in BTO at grown at compressive (111)-strain larger than 1.75% disappears after going through a ferroelectric-to-paraelectric phase transition. The study finds agreance between these calculations and empirical results on superlattices of BTO and STO, where the BTO is said to be compressively strained at 1.5%, and the ferroelectric response is measured to be is very small but non-zero at $1.35\mu C/cm^2$. This is a reduction from the bulk value by a factor of 20. It further goes on to state that tensile strain on (111) strained BTO is needed to enhance the polarization of the BTO in heterostructures. The out of plane polarization for such heterostructures was shown to increase even for high tensile strain states (3%) for both R3m and Cm phases. These results were found using the local density

approximation in Density Functional Theory.
For application in thin films, the study of how these materials are affected by strain in the (111) planes is also of technological importance. Recent studies have indicated that ferroelectric materials with hexagonal crystal structures, such as hexagonal manganites, can display hexagonal vortex domain generation. These vortex domains are believed to make magneto-electrically coupled multiferroic heterostructures a possibility, as the vortex domains are highly unstable and can be influenced by external fields [22]. In combination with other functional oxides showing properties like colossal magneto-resistance in (111) oriented crystals[13], the promise of functional oxide heterostructures with multiferroic, magneto-electric response is promising. Perovskite BTO shows hexagonal *R3m* symmetry when grown along the (111) direction, and as it is one of the prototypical perovskite ferroelectrics and one of the most common ferroelectrics known to date [23], making these vortex domains possible in BTO would be important for the feasibility of producing multiferroic heterostructures for industrial purposes.

1.2 Rationale

Since its discovery in the 1940's, the ferroelectric property of $BaTiO_3$ (BTO) has been one of the best candidates out of the lead-free alternatives [24]. Especially due to the interchangeability of perovskite oxides, BTO make an excellent candidate to be stacked in heterostructures with other perovskite oxides, like ferromagnetic $La_{1-x}S_xrMnO_3$ (LSMO), and rising to the benchmark of the best ferroelectrics, $PbTiO_3$ (PTO) as a viable, lead free alternative. However, most of the breakthroughs concerning ferroelectric films have been on structures grown in the [001] direction. Understanding how other strain directions along with symmetry and strain amount effects the favourability of the phases of BTO, can make these multiferroic, magneto-electrically coupled hetrostructured LSMO/BTO stacks a possibility. In my work on this master thesis, I will examine stuctures of BaTiO3 (BTO) using Density Functional Theory, with particular interest in studying how the crystallographic direction of the interface affects ferroelectric polarization. Ferroelectric perovskites grown along the (111) direction might be important for technological application, as they show hexagonal *R3m* symmetry. Due to the ABO_3 structure, perovskite structures oriented in the (001) direction form alternating layers of BO_2 and AO planes, while in (111) oriented structures the layering consists of alternating B and AO_3 planes. The changing of the chemical and physical interaction between the ions due to strain orientation may open for changed functionality and new applications. Determining how the ferroeletric behaviour in (111)-oriented materials is changed by orientation and strain is thus of relevance.

Chapter 2

Theory

The scope of this chapter is to lay the theoretical foundation for the applications and further discussions described in subsequent chapters. In section 2.1 the important aspects of ferroelectric materials will be presented. In section 2.2 and section 2.3, the significance strain and directionality of the interface will be discussed. section 2.4 will discuss the properties of perovskites and explore the importance of perovskite oxides to the realization of ferroelectric materials, focusing on $BaTiO_3$.

In section 2.5, we will consider density functional theory, describing the fundamental theoretical lines needed to understand the applications in the following chapters. Finally section 2.6 will delve into the modern theory of polarization with special weight on the theory behind the Berry phase analysis of polarization.

2.1 Ferroelectrics

2.1.1 Historical context

The ability for materials to display a temperature-dependent spontaneous electric polarization, known as the *pyroelectric effect*, has been known since ancient times [17]. Attempts to understand and categorize this effect in the eighteenth and nineteenth centuries lead to the discovery of the *piezoelectrisity*, a more general effect where a polarity of a material is induced by a change in the stress of the material. None of the first discovered pyroelectric materials showed *ferroelectric* properties, where the polarizations is spontaneous and re-orientable.

This was mainly due to domain formation in ferroelectrics, hiding the effect on a macroscopic level. The effect went unknown until 1920, when it was discovered that the dielectric response of Rochelle salt to an external electric field was analogous to the ferromagnetic response in iron to applied magnetic field, as a hysteresis would appear in the field-polarization curve. For the first decades the effect was understood as a result of dipole interaction between water molecules in the crystal.
In the 1930's the first *series* of isomorphous ferroelectrics were fabricated, namely phosphates and arsenates, where the principal example is potassium dihydrogen phosphate (KDP), KH_2PO_4. These new materials have only two formula units per primitive cell, simplifying the understanding of the ferroelectric effect from the 112 atom unit cells of Rochelle salt. There is no water of crystallization in KDP, but there are hydrogen bonds where different orientations of the $(H_2PO_4^-)$ dipolar units can result in net polarization of the unit cell. This became the first microscopic model of ferroelectrics able to withstand the test of time [17]. Ferroelectrics were nonetheless considered a rarity in nature, and the apparent necessity of the presence of a hydrogen bond resulted in little interest in looking for ferroelectricity in materials such as oxides.
Titania had been considered a good contender for materials with high dielectric constant. In the studies of $BaTiO_3$ it turned out that it was not only highly dielectric, but also ferroelectric at room temperature. The discovery of ferroelectric response in $BaTiO_3$ in 1945 represented important advances in the field of ferroelectrics, as it was the first ferroelectric without hydrogen bonds, with more than one polar phase, and with a paraelectric prototype phase. As a result of the simplicity of the structure and the chemical an mechanical stability, BTO became the most used ferroelectric and was extensively researched. It became the prototype in the largest class of ferroelectrics known to date: The oxygen octahedral ferroelectrics. Other perovskites like $KNbO_3$, $KTaO_3$, $LiNbO_3$, $LiTaO_3$ and $PbTiO_3$ were found to be ferroelectric in the following years. The microscopic model became one of displacement. Especially for perovskites like BTO, with high *tolerance factor*, the model of the oversized Ba^{2+}-lattice expanding the oxygen octahedra and the Ti^{4+} ion would have ample room to rattle inside it.

With the modern theory of polarization, see section 2.6, the understanding of the ferroelectric effect has been increased to become a quantum mechanical phenomenon. Even though oxides like $PbTiO_3$ have shown stronger ferroelectric effect, $BaTiO_3$ has been the prototypical ferroelectric oxide up until present day.

2.1.2 Ferroelectric crystal systems

As the ferroelectric effect can be understood as a net displacement of charge, the unit cell of the crystal structure can not be centro-symmetric. This eliminates 11 of the 32 possible crystallographic point groups. In addition the 432 cubic class is non-centro symmetric but also not piezo electric. The 20 point groups that

remain are all piezoelectric point groups, and develops a surface electric charge when subject to strain. Further we can eliminate the 10 point groups having no unique polar axis. The 10 remaining point groups all are pyroelectric, and are characterized by a spontaneous charge even in the absence of any electric field or strain. Ferroelectrics are a subgroup of the pyroelectric materials, having the additional criterion that the spontaneous charge must be switchable [25]. Graphing the potential energy of the displaced atom as a function of the location along the polar axis will result in a graph consisting of two ground states separated by a barrier energy, ΔU, known as a dual well, see Figure 2.1.

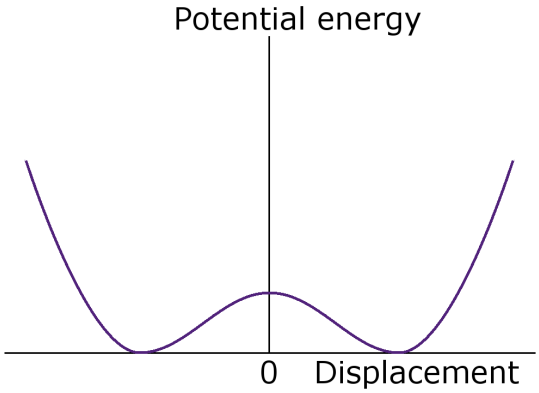

Figure 2.1: Schematic of the dual well in the potential energy for a ferroelectric as a function of displacement of the cation in an anion octahedron. ΔU signifies the energy barrier needed to flip the polarization by moving the cation between the two minima.

Ferroelectrics are defined by this hysteresis response, see Figure 2.2. The field needed to flip the polarization is known as the coercive field, E_C, and the spontaneous polarization is noted as P_S.

In a simplified macroscopic model the loop can be imagined as a result of moving a charged ion between the wells in the energy, where E_C is the field needed to clear the barrier. A further investigation of the modern theory of polarization is found in section 2.6

2.1.3 Domain generation

The ordering of all the microscopic ferroelectric dipoles in a material determines how the ferroelectric property can be utilized. To minimize free energy, dipoles

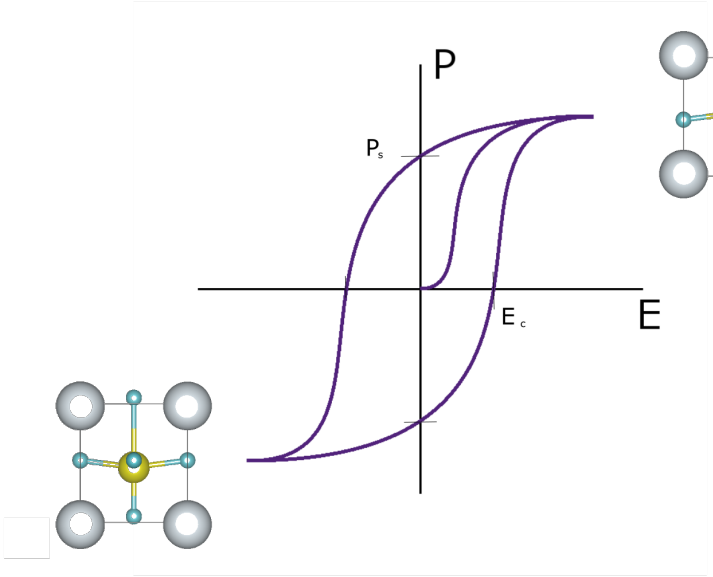

Figure 2.2: Schematic of a hysteresis response in a ferroelectric material. P_S signifies the spontaneous polarisation in the material with no applied field, and E_C is the coercive field needed to reorient the polarization.

on a microscopic scale tend to line up with local dipoles, creating regions in the material where the polarization is uniform. These regions are called domains. In bulk material free energy is minimized by aligning domains in a way to minimize the macroscopic electrical field strength, and with it the energy associated with maintaining a large electric field. This energy is called a depolarization energy. Domain generation is therefore driven by two forces. Microscopically, the dipoles favor aligning with local dipoles, while macroscopically the free energy is minimized by limiting the domain size. There also is an energy cost associated with maintaining the domain wall. This cost is large in head-to-head domain walls and less in anti-parallel walls. Domains in a material will therefore tend to align side by side, anti-parallel to the neighbouring domains, as this minimizes the depolarization field leaving the material in addition to generating energetically cheap domain walls. These domains help in minimizing the depolarization field created by electric field lines leaving the material. The domain structure is also determined by the symmetry requirements of the material. For cubic materials with polarization along the $\langle 001 \rangle$ directions, the domains will meet in angles that are a multiple of 90°. In hexagonal materials, where the polar axes has three-fold symmetry, the domains will generate domain walls meeting at multiples of 120°.

2.1.4 Interface effects

The presence of an interface will influence the domain generation and ultimately the ferroelectric effect in a material. The same depolarization field that limits domain size will make domains facing the interface less favored, as this will create a depolarization field. This is especially important for thin films, as the in plane polarization directions will be much more favored than the out of plane polar axes. The defavorization of out of plane polar axes is also influenced by the favorability of aligning dipoles head to tail locally. In a thin film there is little or no possibility to align dipoles head to tail out of the plane.

2.2 Epitaxial Strain

Macroscopic and microscopic effects can lead to stress on a crystal structure, prompting a deformation from the bulk structure. A strain, ϵ, in a material is the percentwise elongation of a spatial dimension as a result of this stress, defined by Equation 2.1

$$\Delta\varepsilon = \frac{\Delta l}{l_0} \tag{2.1}$$

For a given material, the amount of strain a stress will induce is determined by Hooke's law, Equation 2.2

$$\sigma = E\varepsilon, \tag{2.2}$$

where E is the Young's modulus, defined as the slope in the stress-strain graph [25]. For all stresses smaller than the yield point, the relation is linear and E is constant. If this is the case, the material is considered "Hookean". As the stress increases, the material will approach a yield point where the structure raptures, breaks or irreversably deforms.
Near the crystal-substrate interface, the lattice parameter of the substrate is adopted by the crystal. The mismatch in lattice parameter between a crystal structure and the substrate it is grown on is a typical source for stress and thereby strain. This can induce vacancies or defects, where the crystal will have structural defects to compensate for the shear strain induced by the substrate. The crystal will relax over a distance and revert to its bulk parameters sufficiently far from the substrate interface. For a thin film, the thickness of the film is less than this coherence length. The film will therefore adopt the lattice parameter of the substrates in the planes parallel to the interface, and relaxing in the orthogonal

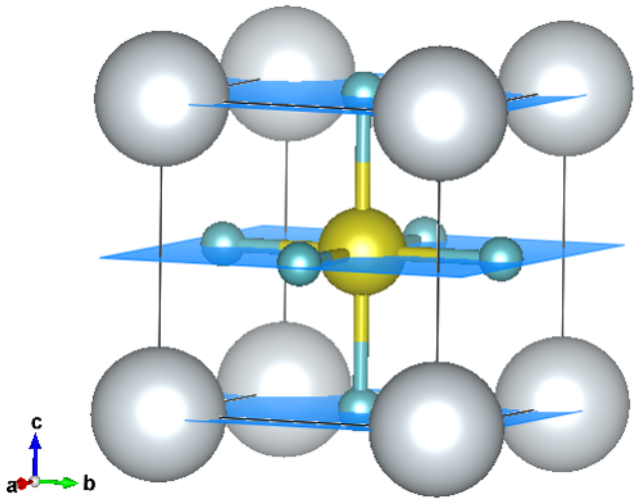

Figure 2.3: When a ⟨001⟩-grown BTO perovskite crystal is submitted to epitaxial strain, the chemical composition of the planes that are strained is alternating BaO and TiO2 planes.

dimension. The strain for thin films becomes the mismatch between the lattice parameters of the bulk crystal and the substrate it is grown on.

2.3 Interface directionality

The directionality of the crystal interface has both applicational and functional significance. When a crystal structure is submitted to strain, the structure will cope with the changed lattice parameter by relaxation, tilting of oxygen octahedra, changing orbital directionality. For a thin film, the crystal will be submitted to epitaxial strain in planes perpendicular to the direction of the growth, to compensate for the mismatching lattice parameter of the crystal and the substrate structure. The directionality of the plains can influence the structure's ability to compensate for the strain. The disability to compensate for strain can change the favourable phases of the material at different temperatures, altering the phase diagram. Due to the ABO_3 structure, perovskite structures oriented in the (001) direction form alternating layers of BO_2 and AO planes as shown in Figure 2.3, while in (111) oriented structures the layering consists of alternating B and AO_3 planes, Figure 2.4.

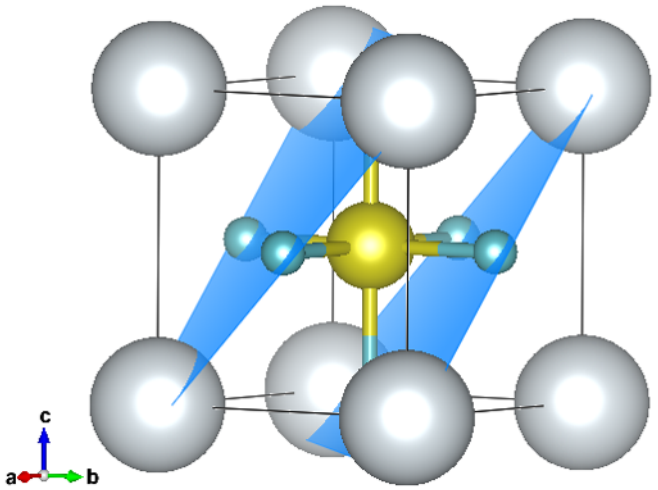

Figure 2.4: When a ⟨111⟩-grown BTO perovskite crystal is submitted to epitaxial strain, the chemical composition of the planes that are strained is alternating BaO3 and Ti planes.

In addition to changing the functionality, the direction of the crystal growth will influence the ability to create interfaces with other materials, which has influence on the application.

2.4 Perovskites

Perovskites has been one of the most active areas of research within material science and solid state chemistry during the last decades due to the numerous interesting properties that derives from the different possibilities in the structure. [26] Among the properties shown is ferroelectricity, where $PbTiO_3$ (PTO) and $BaTiO_3$ (BTO) have been the prototypical examples. [25] The structure gets its name from the mineral perovskite, $CaTiO_3$, and has a characteristic ABX_3 unit formula. The A-site cations create a pseudocubic unit cell, with face centered X-site anions and a body centered B-site cation, see Figure 2.5. Generally A-site ions are alkaline or rare earth elements, B-site ions are transition metals, and generally the X-sites are occupied by oxygen. The structure is very versatile, and most elements can be incorporated in a perovskite structure at either the A or B-site, creating a large variety of possible materials and applications.

A defining characteristic of a perovskite crystal is the tolerance factor, t. The accuracy of the factor is disputed, but it gives some insight into the behaveour of perovskites with varying elemental constitution. Equation (2.3) is derived from equating the sizes of the cubic close packed layers of the perovskite structure with the relative ionic sizes. t is any deviation from this perfect size matching, as given by equation (2.4).

$$a = \sqrt{2}(R_A + R_X) = 2(R_B + R_X) \tag{2.3}$$

$$t = \frac{R_A + R_X}{\sqrt{2}(R_B + R_X)} = \frac{d_{AX}}{\sqrt{2}d_{BX}} \tag{2.4}$$

where R_A, R_B and R_X are the ionic radii of the A, B and X-site ions, and d_{AX} and d_{BX} is the preferred inter-atomic distance between A and X and B and X, respectively. Even though the tolerance factor is somewhat approximate, it indicates the possible strain in the structure due to the mismatch of the ionic radii. A tolerance factor close to unity, generally between 0.9 and 1.0 [27], signifies good or perfect radii matching. Structures with a good lattice matching will give cubic or pseudocubic structures and phases with limited octahedron tilting. $SrTiO_3$ (STO) is the prototypical example of such a crystal, as STO is cubic at room temperature. As a result of this, STO is the presumed substrate for most thin film applications using functional oxides due to the regularity a perfectly cubic system gives. A tolerance factor less than 0.9 will result in tilting of the octahedra, as A-site ions want to shorten the covalent bond lengths, however a tolerance factor between 0.8 and 0.9 will still be considered good for cubic perovskites [27] The tilting of the octahedra lead to orthorhombic and rhombohedral crystal systems. The tilting also suppresses ferroelectric responses [23]. A tolerance factor larger than unity generally results in hexagonal crystal systems [27], however there are notable exceptions, BTO being one of them.

2.4.1 $BaTiO_3$ - Structure and ferroelectric properties

$BaTiO_3$ (BTO) is the most common ferroelectric oxide in the perovskite structure [29]. It occurs in four pseudocubic phases, of which the tetragonal is the most stable at room temperature ($5°C < T < 120°C$), see Table 2.1.

In the tetragonal phase, the polar axis is parallel to one of the pseudocubic lattice parameters, as one of the axes are stretched from the cubic state. Empirically, the lengths of the lattice parameters in the BTO tetragonal phase is found to be a$\approx$ 0.3956 nm and c $\approx$ 0.4035 nm, giving c/a $\approx$ 1.02. There is no preference as to which crystallographic axes becomes the polar direction, meaning that there are

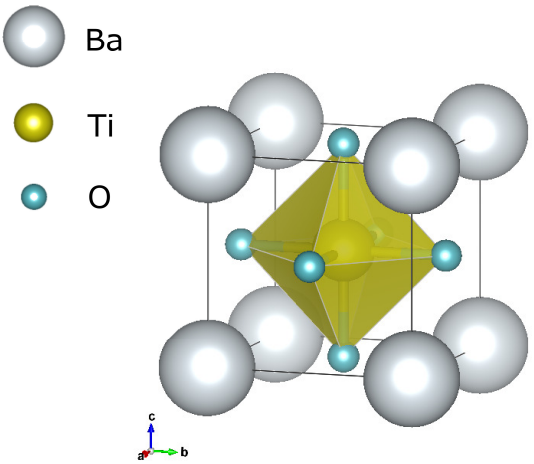

Figure 2.5: The unit cell of perovskite $BaTiO_3$ in the cubic phase [28].

Table 2.1: Temperature region, point group and polar axis for the four perovskite phases of $BaTiO_3$. [17]

Phase	Temperature	Point group	Polar axis
Cubic	Above 120°C	m3m	Non-polar
Tetragonal	5°C to 120°C	mm4	⟨001⟩
Orthorhombic	-90°C to 5°C	mm	⟨011⟩
Rhombohedral	Below -90°C	3m	⟨111⟩

three equivalent polar axes, and six equivalent polar directions. [25] For lower temperatures, BTO undergo phase transitions to orthorhombic (-90°C < T < 5°C) and rhombohedral (T < -90°C) phases, both of which also show ferroelectric responses. For the orthorhombic phase, the displacement is along the pseudocubic ⟨011⟩-direction, and for the rhombohedral the displacement is along the ⟨111⟩-direction. The valency of the constituent ions are Ba^{2+},Ti^{4+} and O^{2-}, with interionic distances $d_{BaO} = 2.953$, $d_{TiO} = 1.965$. This gives a tolerance factor of 1.063, (2.5)

$$t = \frac{2.953}{1.965\sqrt{2}}. \tag{2.5}$$

The tolerance factor being slightly higher than 1 indicates that the A-site Ba^{2+} cations are over-sized compared to the Ti^{4+} B-site cations. The ferroelectric

property of BTO has been described as stemming from this discrepancy in size, however it is a somewhat oversimplified model. [25] In the best ferroelectric perovskite, $PbTiO_3$ (PTO), the ferroelectric effect is explained by the hybridization of lead and oxygen states, straining the material and stabilizing the tetragonal phase and the charge displacement. In contrast, the barium and oxygen in BTO interaction is completely ionic [24], and even though the tolerance factor is further from unity, the c/a is lower.

Table 2.2: Experimental data on lattice parameters and volume for the four phases of $BaTiO_3$. [30]

Phase	a[Å]	b[Å]	c[Å]	α=β=γ[°]	Volume [Å^3]
Cubic[31]	4.008	4.008	4.008	90	64.38
Tetragonal [32]	3.9972	3.9972	4.041	90	64.57
Orthorhombic [33]	3.98	4.01	4.02	$\tilde{9}0$	64.16
Rhombohedral [34]	4.0036	4.0036	4.0036	89.839	64.17

2.5 Density Functional Theory

This section will seek to introduce the theoretical background of density functional theory (DFT). DFT is a quantum mechanical method to solving the Schrödinger equation numerically. As the energy functional for the electron density maps the ground state of the Schrödinger equation, the many-body problem is simplified to a function with three degrees of freedom. Numerical methods is used to relax the system to its lowest energy state, equalling the ground state energy for the crystal structure. DFT allows for the derivation of properties like ferroelectric polarization, crystal structure and magnetic properties on length scales difficult to achieve experimentally, and is an appropriate tool for examining the structures in question [35].

2.5.1 The Schrödinger Equation

Traditionally to find the ground state energy for any quantum mechanical system one would have to apply the Hamiltonian on the wave function to get the time independent Schrödinger equation Equation 2.6 [36]

$$H\psi = E\psi, \tag{2.6}$$

where H is the Hamiltonian operator, E is the energy eigenvalue and ψ is the wave

function. For a single electron the Hamiltonian includes one term concerning the kinetic energy and one concerning potential, Equation 2.7

$$-\frac{\hbar^2}{2m}\frac{d^2\psi}{dx^2} + V\psi = E\psi, \tag{2.7}$$

where V is the nuclei potential, m is the mass of the particle and $\hbar$ is the reduced Planck constant. Single particle problems are instructive in understanding the simple interactions between electron and nucleus but hold little value when tasked with problems concerning atoms, crystal structures and nano particles. To solve these problems a generalized version of the time independent Schrödinger equation where each term is a summation of the contribution from all N particles in the system is used:

$$\Big[-\frac{\hbar^2}{2m}\sum_{i=1}^{N}\nabla^2 + \sum_{i=1}^{N}V(\mathbf{r_i}) + \sum_{i=1}^{N}V_H(\mathbf{r_i})\Big]\psi = E\psi. \tag{2.8}$$

When considering a many-body problem, we now also must take the electron-electron repulsion into account. This repulsion gives rise to the Hartree potential, V_H. In a bulk material the number of electrons, N, becomes large and solving the many-body problems needed to analyse the potential functionalities of a material becomes exhaustive. DFT is a method to reduce the dimensionality of the problem to make computational analysis manageable.

2.5.2 DFT fundamentals

The field of Density Functional Theory is built on a body of work done in the latter half of the 20th century, resulting in two theorems by Hohenberg and Kohn [35]. The first Hohenberg and Kohn-theorem states that there exists an energy functional giving a one-to-one mapping between the resulting value of the electron density and the wave function ground state. This mapping has profound effects on the computational power needed to find the ground state of materials and particles with well defined atomic positions: As a result of the relative mass difference between atom nuclei and electrons, a crystal system can be simplified to a fixed ionic lattice and a sea of electrons constantly moving around. Still with this simplification, the simplest case of a $BaTiO_3$ structure will give a Schrödinger equation with 306 dimensions, three dimensions for each of the 102 electrons in the unit cell. Density functional theory utilizes the electron density functional's ability to produce a one-to-one mapping of the wave function energy ground state, simplifying the problem from an equation with 102 variables to only considering the electron density, a function in three dimensions: [37]

$$n(\mathbf{r}) = 2\sum_{i=1}^{120} \psi_i^*(\mathbf{r})\psi_i(\mathbf{r}) \tag{2.9}$$

Hohenberg and Kohn's second theorem imposes an important property on the electron density corresponding to the true ground state: The electron density that minimizes the energy of the overall functional is the true electron density corresponding to the full solution of the Schrödinger equation. [35] This means that the ideal electron density can be found by minimizing the result of the electron density functional.

The energy functional used are derived from the Kohn- Sham equations

$$\left[-\frac{\hbar^2}{2m}\nabla^2 + V(\mathbf{r}) + V_H(\mathbf{r}) + V_{XC}(\mathbf{r}) \right] \psi_i(\mathbf{r}) = \epsilon_i \psi_i(\mathbf{r}) \tag{2.10}$$

where V and V_H are the nuclei and Hartree potentials from the Schrödinger equation respectively, and V_{XC} represent the exchange and correlation residuals. The first two are well-defined, while the latter is a collection of all the unknown potentials and corrections for e.g. compensation for self-repulsion included in V_H. The complete analytical energy functional is therefore unknown, so in stead approximate forms are used. These approximations vary in sophistication, complexity and accuracy. In the work outlined in this report, *local density* (LDA) and *generalized gradient* (GGA) approximations have been utilized. Local density approximation assumes the exchange correlation potential scales linearly with the local electron density, giving

$$V_{XC}(\mathbf{r}) = V_{XC}^{\text{electron gas}}[n(\mathbf{r})] \tag{2.11}$$

where $V_{XC}^{\text{electron gas}}$ is the electron gas potential. This is considered the crudest of the approximations but it has been shown to be accurate for certain systems. The generalised gradient approximation also takes into account the local gradient of the electron density. As the GGA can not be done uniquely, there are many variants of GGA functionals, varying in the implementation of the gradient component. The GGA functional used in this work has been a variant of the Perdew–Burke–Ernzerhof (PBE) functional, PBEsol, revised for solids.

2.5.3 Using DFT

Finding the energy minimum is an iterative process, relying on algorithmic procedures. [35]

1. An initial guess of the crystal structure and the corresponding electron density is made and fed into the electron density functional.

2. Solve the Kohm-Sham equations.

3. Find the electron density corresponding to the Kohn-Sham equations.

4. Compare output and input, and measure against convergence criteria.

5. Repeat from step 2 if the calculation is not yet converged.

This process is iterated until the specified precision is reached. In VASP the precision is determined by the EDIFF and EDIFFG tags. Generally this is referred to as being self-consistent or converged. The level of convergence relies on the calculations including enough information to correctly and reliantly find the energy minimum. A well converged calculation has found the correct energy minimum.

2.6 Berry Phase Analysis

2.6.1 The modern theory of polarization

The modern theory of polarization arose from the contradictory nature of the classical description of periodic solids. Classically, the polarization is understood to be a displacement of the ions in a solid, and by adding up the charge distribution in a given volume, the total polarization per unit volume could be derived. However when considering periodic solids, the same structure can give a plethora of valid polarization values dependent upon what unit volume is considered. Consider a one-dimensional row of alternating positive and negative charges, Figure 2.6.[38] Since the material is repeating, one is free to chose any cell to integrate the charge distribution over as long as one integrate over a whole multiple of unit cells. By choosing the two different unit cells shown in Figure 2.6 we get both Equation 2.12 and Equation 2.13, where a is the unit cell parameter, x_i is the position and q_i is the charge.

$$p = \frac{1}{a}\sum x_i q_i = \frac{1}{a}(-1 \times \frac{a}{4} + 1 \times \frac{3a}{4}) = \frac{1}{2} \tag{2.12}$$

$$p = \frac{1}{a}\sum x_i q_i = \frac{1}{a}(1 \times \frac{a}{4} - 1 \times \frac{3a}{4}) = -\frac{1}{2} \tag{2.13}$$

We see that by shifting this unit cell by one half unit cell parameter we can see that the same structure can give two or more valid solutions to the polarization, whereas in reality, there ought to be a unique answer. Fundamentally this problem boils down to the definition of polarization. It seems that the polarization of a periodic solid is not well-defined, and has an infinite set of valid values. Only the *change* in polarization has a well-defined value, as it can be derived no matter what unit cell position is chosen, as we see in Equation 2.14 and Equation 2.15

$$p = \frac{1}{a}\sum x_i q_i = \frac{1}{a}(-1 \times \frac{a}{4} + 1 \times (\frac{3a}{4} + d)) = \frac{1}{2} + \frac{d}{a} \tag{2.14}$$

$$p = \frac{1}{a}\sum x_i q_i = \frac{1}{a}(1 \times (\frac{a}{4} + d) - 1 \times \frac{3a}{4}) = -\frac{1}{2} + \frac{d}{a} \tag{2.15}$$

When subtracting Equation 2.12 from Equation 2.14 and Equation 2.13 from Equation 2.15 we se that we get $\frac{d}{a}$ in both cases. The results in Equation 2.12 and Equation 2.13 are one *polarization quantum*, p_q, apart at $+\frac{p_q}{2}$ and $-\frac{p_q}{2}$ respectively. The polarization quantum represent the value added to a polarization calculation by moving one charge one whole unit cell. The polarization quanta are calculated by Equation 2.16, where a_i is the lattice parameter, Ω is the unit cell volume and C is a conversion constant.

$$p_{qi} = \frac{a_i C}{\Omega} \tag{2.16}$$

$C = 1602.176462 \frac{\mu C/cm^2}{e/\mathring{A}^2}$

As the quantum is dependent on the lattice parameter, each of the three Cartesian directions will have a polarization quanta associated with it, giving a *polarization lattice* of viable polarization values. Finding the correct value comes down to adding the correct amount of polarization quanta in each direction. In practice the calculations are done with intermediate steps to ensure that the calculations are on the same *branch* of the polarization lattice, as seen in Figure 2.8 [38].

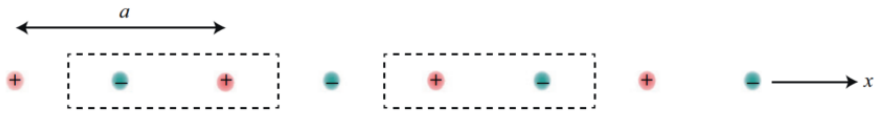

Figure 2.6: A chain of charges analysed by two different unit cells [38].

2.6.2 Born Effective charge

In addition to the contribution from the ionic displacement we need also consider the electronic displacement as a function of the displacement of the ions. Consider again the row of alternating charges, and substitute their mathematical point-charge by a real-world ions of Na^+ and Cl^-. By moving the positively charged Na^+ in the positive x-direction, it attracts the negatively charged electron cloud around the Cl^--ion, see Figure 2.9. When calculating the final value of the polarization we need to also account for the movement in the negative direction of negative charges, that contribute considerably to the total charge displacement. We find that the resulting charge displacement can be approximated by an *effective charge*. For most solids the Born effective charge contribute to the ions having a bigger charge contribution than the formal charges.

Quantifying these electronic contributions is done by Wannier functions Equation 2.17 [38]

$$\begin{aligned} w_n(\mathbf{r}-\mathbf{R}) &= \frac{\Omega}{(2\pi)^3}\int_{BZ} d^3\mathbf{k} e^{-i\mathbf{k}.\mathbf{R}}\Psi_{n\mathbf{k}}(\mathbf{r}) \\ &= \frac{\Omega}{(2\pi)^3}\int_{BZ} d^3\mathbf{k} e^{-i\mathbf{k}.(\mathbf{r}-\mathbf{R})}u_{n\mathbf{k}}(\mathbf{r}) \end{aligned} \tag{2.17}$$

where $\Psi_{n\mathbf{k}}(\mathbf{r}) = e^{i\mathbf{k}.\mathbf{r}}u_{n\mathbf{k}}(\mathbf{r})$ are the Bloch function substitution done for periodic solids and Ω is the unit cell volume. The Wannier functions are, unlike Bloch functions, centralized. The center of the distribution is calculated by averaging the position of the electron distribution and is called the Wannier center, $\bar{\mathbf{r}}_n$. The total polarization is found by summing the contribution for the displacement of both point charge ions and the Wannier centers:

$$p = \frac{1}{a}\left(\sum_i (q_i x_i)^{ions} + \sum_n^{occ}(q_n \bar{\mathbf{r}}_n)^{WFs}\right) \tag{2.18}$$

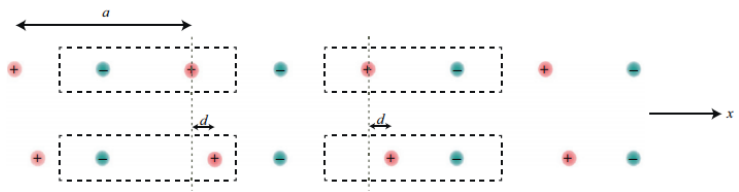

Figure 2.7: A change in polarization in a chain of charges analysed by two different unit cells.[38]

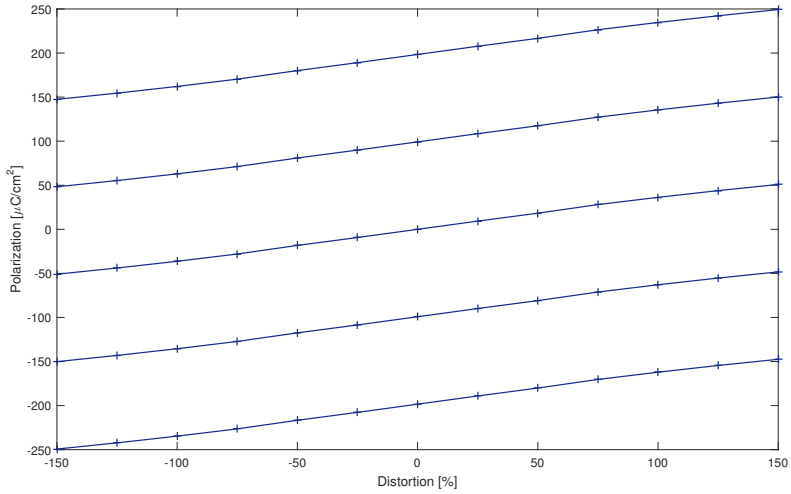

Figure 2.8: Schematic of the branches in the polarization lattice. To ensure the right polarization value is obtained, the change in polarization from a centrosymmetric unit cell along a single branch is used, as this is a uniquely defined value.

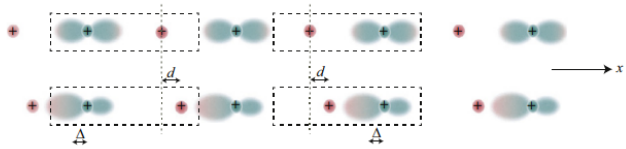

Figure 2.9: A change in polarization in a chain of charged ions analysed by two different unit cells [38].

2.6.3 The Berry Phase

A quantal system in an eigenstate transported slowly round a closed circuit C by changing the spatial parameters $\mathbf{R}$ in the Hamiltonian $\hat{H}(\mathbf{R})$ will acquire a phase factor $exp\{i\gamma(C)\}$ in addition to the dynamic phase factor known as the *Berry phase* [39]. The electronic contribution to the difference in polarization can be described by the Berry phase of a finite adiabatic change in the Kohn-Sham Hamiltonian of the system, see Equation 2.10.

$$\Delta \mathbf{P}_e = \int_{\lambda_1}^{\lambda_2} \frac{\partial \mathbf{P}_e}{\partial \lambda} d\lambda \tag{2.19}$$

$$\frac{\partial \mathbf{P}_e}{\partial \lambda} = \frac{i|e|\hbar}{N\Omega_0 m_e} \sum_{\mathbf{k}} \sum_{n=1}^{M} \sum_{m=M+1}^{\inf} \frac{\langle \psi_{n\mathbf{k}}^{(\lambda)} | \hat{\mathbf{p}} | \psi_{m\mathbf{k}}^{(\lambda)} \rangle \langle \psi_{m\mathbf{k}}^{(\lambda)} | V^{(\lambda)} | \psi_{n\mathbf{k}}^{(\lambda)} \rangle}{(\epsilon_{n\mathbf{k}}^{(\lambda)} - \epsilon_{m\mathbf{k}}^{(\lambda)})^2} + c.c. \qquad (2.20)$$

where m_e and e is the mass and charge of the electron respectively, Ω_0 is the unit cell volume, N is the number of unit cells in the crystal, M is the number of occupied bands, $\hat{\mathbf{p}}$ is the momentum operator and $\psi_{n\mathbf{k}}^{(\lambda)}$ are the Bloch solutions of the crystalline Hamiltonian. Using DFT, $V^{(\lambda)}$ is substituted with the Kohn-Sham potential, $V_{KS}^{(\lambda)}$ [40]. For simple cases, the Berry phase integrals simplify to the Wannier fuctions [38].

Chapter 3

Methodology

This chapter detail the methodology used to obtain the results discussed in chapter 4. Firstly section 3.1 will outline the process of performing DFT calculations using the Viena Ab-initio Simulation Package (VASP) [41–44], detailing the files needed and specifics on the settings used to perform the calculations in this thesis. This section will also contain result from the preliminary calculations sone in my project work [45], and lay out the reasoning for setting certain variables for later calculations. In section 3.2 the specifics of the volumetric relaxations done is laid out. section 3.3 outlines the methods used to set up and carry out calculations on strained crystals of BTO with both (001) strain and (111) strain. finally, section 3.4 describes how the Berry phase analysis of all the relaxed volumetric and strained samples were done.

3.1 DFT

The data for this thesis result from Density Functional Theory (DFT)-calculations, using the Viena Ab-initio Simulation Package (VASP) [41–44]. VASP initializes the calculations using input files, outlying the limits of the calculation. The VASP software can accept a lot of input files, but at the very least four input files are needed to run a successful VASP calculation.

- INCAR
- POSCAR
- POTCAR

- KPOINTS

These files serve each their own purpose in initializing and controlling the calculation.

3.1.1 INCAR

INCAR is the central input file of VASP. It determines 'what to do and how to do it'.[46] The INCAR file is a list of variables, called tags. These tags parameters for convergence criteria, select which functional is used for the density approximation, determine the precision of symmetry determination. An example of an INCAR-file is found in section A.1 of Appendix A. The INCAR-file also determine which quantities are calculated. This influences the complexity of the calculation, influencing how long it takes to converge etc.
In the project work leading into this thesis [45] a study of various input values was carried out hoping to determine the appropriate values in order to both get convergence while not wasting CPU hours on needlessly accurate, heavy or complex calculations. As BTO contains oxygen an energy cut-off ENCUT of 550eV is needed. This tag sets the cut of energy for the plane waves considered in the calculations, where all plane waves with a kinetic energy smaller than ENCUT are included in the calculation. An ENCUT of 550ev is fairly high, but for structures containing oxygen it is needed.
In general the calculations in this thesis is done using the PBEsol functional [1, 2]. The exception is for volumetric calculations, where also the LDA functional [5] is used.

3.1.2 POSCAR

The POSCAR file holds the lattice parameters and structure of the unit cell in addition to the position and element of all the atoms in it. The POSCAR files are generated using VESTA [28]. An example of a BTO POSCAR file is found in section A.3 of Appendix A. These files are the difference between the calculations done on different phases, and are also the piles manipulated in the strain calculations. This is done by using the script found in **??**. It functions by setting the lattice parameter values needed to correspond to certain strain values. As the ion positions are given by fractional coordinates, only the a and b parameters need to be changed.

3.1.3 POTCAR

The POTCAR file entails a list of the pseudopotential used. The potentials for a crystal structure are concatenated from files containing potentials for individual elements in a catalogue provided by VASP. Most elements have several pseudopotential files, corresponding to different valency and softness levels. The order the potentials are added to the POTCAR must be in accordance with the order they are listed in the POSCAR file, to ensure that the right pseudopotentials are linked to the right element. The POTCAR-files for the work done in this thesis is composed of the potentials listed in **??**

3.1.4 KPOINTS

The KPOINTS file specifies the distributions and density of K points in the Brillouin zone (BZ). The KPOINTS file allows to vary the amount of K-points that occur in each of the three dimensions in reciprocal space, whether the mesh shall be evenly distributed and whether the Gamma point will contain a point, i.e. the mesh is centered in the BZ. An example of a KPOINTS file is found in section A.2 of Appendix A. In the calculations done in this thesis, the K-point density is in the order of 200 per reciprocal unit cell in accordance with the results found in my project work [45]. As the K-points in each direction are integers it is hard to get the K point density constant. In general, the amount of K-points should be halved when the volume is doubled [35]. For the single unit cells used in the strain calculations and volume relaxations, the k-point value has been set to 6 in each direction. As the larger supercells used in the (111) strained calculations are 6 formula units, the amount of K-points is lowered to 3, 4 and 3 to account for the decreased BZ of a larger unit cell.

3.1.5 Other relevant files

In addition to the four essential files, there are other files that can be used to speed up the calculations. One such file is the WAVECAR file, containing information about the electron wave modes in the structure so that VASP is not required to calculate it. This file is also generated by VASP, and is used between consecutive calculations on the same structure, saving VASP the need to calculate the wave functions present in the structure for all the calculations.

3.2 Full volumetric relaxations

The DFT analysis on the volumetric calculations are done with both LDA[5] and PBEsol functional [1, 2]. EDIFF and EDIFFG are set to 1E-6 and 1E-2 respectively. Full volumetric relaxations in VASP are done by setting the ISIF-tag to 3, allowing the algorithm to change the cell volume and shape, along with allowing for the ions to relax.

3.3 Strain calculations

To simulate the application conditions the sample is submitted to cubic strain, meaning the a and b parameters are set equal with a 90 degree angle between them. This is done to simulate the conditions of thin film growth, where the film is grown on a typical cubic substrate like $SrTiO_3$. The cubic strain makes the investigation of which phase is favoured mainly focused on the position of the ions and the polarization direction, as the unit cell has a tetragonal-like shape for all phases. An orthorhombic phase submitted to cubic strain will no longer have $a \neq b \neq c$, and will only be orthorhombic-like in the sense that the polarization direction still will be in the pseudocubic $\langle 011 \rangle$-direction. The strain values are normalized to the lattice constant of the rhombohedral phase found in the volumetric relaxation, as this is the lowest energy phase.

The strain calculations differ from normal volumetric relaxations in the allowed amount of volumetric relaxation using a mode of the VASP software called vasp-ab-fix.x. Using this mode, the structure is prohibited from relaxing in the ab-plane, whereas the c-parameter can relax freely. In addition the angle of the lattice parameter out of the strain plane is set constant at 90 degrees. The ions can relax freely, and with them also the polarization direction and magnitude. To initialize crystals with strain in the (111) plain, the supercell entered in the POSCAR file must have the $\langle 111 \rangle$ direction along the POSCAR c-axis. This is done by rotating the unit cell of the various phases in VESTA using a set of transformation matrices.

$$\begin{array}{ccc} \text{rectifying} & \text{[111] rotation} & \text{[001] cell} \\ \begin{bmatrix} 1 & -1 & 0 \\ 1 & 1 & 0 \\ 0 & 0 & 1 \end{bmatrix} & \begin{bmatrix} -1 & 0 & -1 \\ 0 & 1 & -1 \\ 1 & -1 & -1 \end{bmatrix} & \begin{bmatrix} a & 0 & 0 \\ 0 & b & 0 \\ 0 & 0 & c \end{bmatrix} \end{array}$$

$$\begin{array}{ccc} \text{rectifying} & \text{[11-1] rotation} & \text{[001] cell} \\ \begin{bmatrix} 1 & -1 & 0 \\ 1 & 1 & 0 \\ 0 & 0 & 1 \end{bmatrix} & \begin{bmatrix} 1 & 0 & 1 \\ 0 & 1 & -1 \\ -1 & 1 & 1 \end{bmatrix} & \begin{bmatrix} a & 0 & 0 \\ 0 & b & 0 \\ 0 & 0 & c \end{bmatrix} \end{array}$$

Because straining the sample breaks the symmetry of the structure, several calculations is done for different rotational permutations of the structures. For instance, the tetragonal phase will relax differently depending on the direction of the extraordinary axis, and if it is in the polarization plane or perpendicular to it. For the calculations done in (111) strained systems, this consideration becomes more important as most of the polarization directions has some non-trivial component of its polarization in the strain plane, making the structures less subject to symmetry degeneration. The two rotation matrices reorients the [111] and the [11-1] to the supercell c-axis respectively with a and b vectors along the $\langle 011 \rangle$ pseudocubic directions orthogonal to the c-axis, resulting in a hexagonal supercell. The rectifying matrix is used to make $\alpha=\beta=\gamma=90°$, simplifying further manipulation of the super cells and processing of polarization. The resulting super cell has 6 formula units as opposed to the single formula unit for the (001) strained cells.

When doing strain calculations it is important to consider how the strain orientation breaks the symmetry. For bulk calculations the orientation of the phase is irrelevant. When straining a sample, the component parallel to the strin plane will react differently to strain than the component out of the strain plane. The tetragonal phase of BTO has a six-fold symmetry, where the extraordinary axis conceivably can be oriented along any of the pseudocubic axes, with the ferroelectric polarization pointing in either the positive or negative direction. For (001) strained crystals this means that there are two orientations to concider: [001] and [100]. As [001] is orthogonal to the strain plane when straining in the ab-plane, it will conceivably relax to another energy and symmetry than the [001] oriented tetragonal phase. However, when the crystal is (111) strained, this consideration changes. Around the [111]-axis, all of the $\langle 001 \rangle$ axes become equivalent, due to an equal 35° angle of polarization with the strain plane. We therefore only need consider one orientation of the tetragonally initialized structures when doing (001) strained calculations.

The bulk polarization of the orthorhombic phase of BTO has a $\langle 011 \rangle$-direction, meaning that the Ti^{4+} is displaced towards one of the edges of the oxygen octahedra, giving 6 polar axes and 12 polarization directions. For (001) strained crystals two of the polarization axes are oriented in the polarization plane, while 4 are oriented partially out of the plane. Given that there is cubic strain, the four out of plane polarizations become equivalent with a 45° agle to the plane, meaning we have to consider two orientations of the orthorhombic phases: one in plane and one partially out of the plane. For (111) strain 3 of the polar axes lie parallel with the strain plane and 3 form an angle with the strain plane of 55 °. The rhombohedral phases have a displacement along the $\langle 111 \rangle$-direction, meaning the ion displacement points towards the faces of the octahedra. For (001) strained crystals the axes become equivalent, and only one rhombohedral ori-

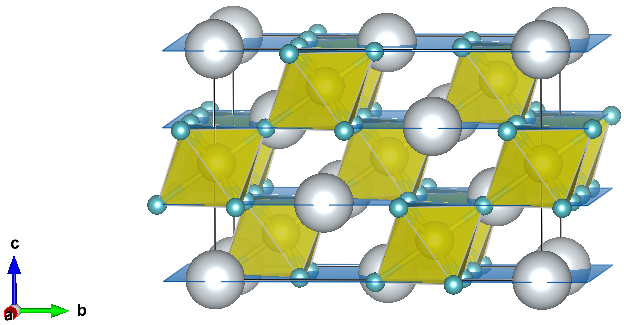

Figure 3.1: An example of a rotated crystal structure, with [111] along the supercell c-axis. The planes marked correspond to the (111) strain planes.

entation needs to be considered. (111) strained rhombohedral phases have two orientations needed to be considered: One with the polarization normal to the strain plane and one where the polarization direction forms a 19° angle with the polarization plane.
All the strain calculations were relaxed with the INCAR-file in section A.1 using PBEsol functional [1, 2] and EDIFF and EDIFFG to 1E-7 and E1-3 respectively.

3.4 Berry phase analysis

To calculate the polarization in a sample using DFT, Berry phase analysis is used. VASP includes the tag LCALCPOL, calculation the total polarization in the supecell submitted to the calculation. In effect VASP integrates the charge density over a unit cell, finding the net charge displacement. Adding this calculation makes the total relaxation more CPU intensive, so for all the results in this thesis the structure is first relaxed with the appropriate amount of freedom, and then a separate polarization calculation is done on the resulting structure, where VASP only allows electronic relaxation. In practice this is done by setting the NSW-tag to 0, as it dictates the amount of ionic steps allowed before the calculation exits the relaxation loop. Both the electronic and ionic polarization values are calculated and added to the OUTCAR-file. The calculations are done with PBEsol functional [1, 2] and and EDIFF and EDIFFG to 1E-6 and E1-2 respectively.

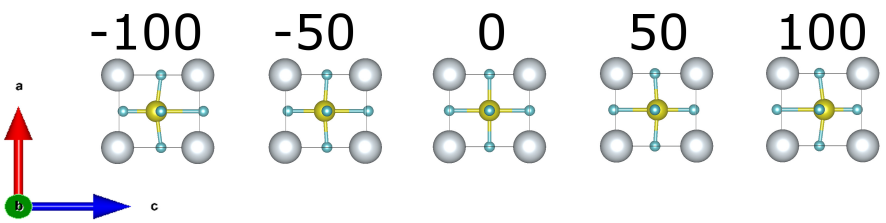

Figure 3.2: The distortion of a unit cell from -100% to 100% via the centro-symmetric reference cell.

When analyzing the effective charge, the ionic and electronic contribution is added together. As discussed in section 2.6, the Berry phase integral has an infinite number of valid results, as the absolute polarization is not uniquely defined, while the *change* in polarization can be quantified uniquely when accounting for polarization quanta. A series of calculations is therefore done where the goal is to measure the change in polarization between a non-polar reference and the sample we want to probe. The calculations are identical, except from the POSCAR-file, see subsection 3.1.2. A reference structure, POSCAR-ref, is made where the ions are placed centro-symmetrically in the correct unit cell. By distorting the unit cell from the reference to the actual structure, POSCAR-pol, by set distances, we can assure that we can account for polarization quanta. As the polarization quanta is defined by the structural parameters of the crystal , Equation 2.16, some structures will have larger P_q than others. To assure the calculated polarization is placed on the correct *branch* of polarization, as seen in Figure 2.8, the steps between the POSCAR-pol and the POSCAR-ref needs to be small enough. For simple unit cells, 25% distortion is chosen. In practise this means that the ions are moved from the high symmetry centro-symmetrical positions to the positions in the structure we want to examine with three equidistant intermediate steps, in addition to extending the distortion to 150% on each side. These calculations are unphysical, but serves as guide to adjust for the correct amount of polarization quanta. Calculations for negative distortion is also carried out. These extend the line beyond the zero point, and even though they might be redundant for the calculations carried out in this thesis they can help discover artifacts and help adjust samples where the Berry phase calculation of the non-polar sample equals one half of a polarization quantum.

The calculated polarization contribution from the ionic displacement and electronic distribution are added together. By dividing by the unit cell volume the total polarization per unit cell volume is found. The final polarization vector is derived by adding the appropriate number of polarization quanta to ensure the polarization at 0% and 100% distortion is on the same branch. [38] This is done separately for each of the spatial directions. The final polarization vector is derived as the vector sum of the polarization along each unit vector. For phases

where the polarization is not aligned with one of the unit vectors it is especially important to ensure that the appropriate amount of polarization quanta are added in each of its spatial components before combining the components because the amount of polarization quanta needed will differ. The calculations are initialized with the initialize script found in Appendix C, and the interpolation between the reference an polar POSCARS are done with the posinterpol.pl-script, also found in Appendix C

Chapter 4

Results and Discussion

Here all the results from the calculations described in chapter 3 will be presented. The chapter will contain the results from the initial calculations from the project thesis, as they serve to explain the importance of choosing parameters values. In section 4.1, the results from the volumetric relaxations will be presented and compared to experimental data.

section 4.2 will contain the results from the strain calculations for both (001) oriented and (111) oriented films. These calculations will be done with higher precision than the ones done in the project thesis.

subsection 4.2.4 will show the results form the berry phase calculations on both relaxed bulk BTO and strained BTO in (001) and (111) planes. These results are included to ensure the polarization in the strained films is as expected in terms of magnitude and direction.

4.1 Full volumetric relaxations

The full volumetric relaxations, were done with both LDA [5] and PBEsol[1, 2] exchange correlations for all four phases. The resulting lattice parameters and unit cell volumes are detailed in Table 4.1 and Table 4.2. The fully relaxed unit cell volume differs between the two exchange correlations. Comparing to experimental data, Table 2.2, we can see that LDA generally underestimates the volumes, while PBEsol have relatively good accordance with the experimental data, although slightly overestimate the experimental values. However, the relative energy differences between energies calculated with the same approximation

Table 4.1: Relaxed unit cell parameters for all four phases of BTO using LDA. For the full relaxations, all the angles α, β and γ are equal.

Phase	a [Å]	b[Å]	c [Å]	α=β=γ[°]	Volume [Å^3]
Cubic	3.92074	3.92074	3.92074	90	60.2706311
Tetragonal	3.91655	3.91655	3.93474	90	60.3563364
Orthorhombic	3.91653	3.92603	3.92792	90	60.3972963
Rhombohedral	3.92403	3.92403	3.92403	89.98	60.4222479

Table 4.2: Relaxed unit cell parameters for all four phases of BTO using PBEsol. For the full relaxations, all the angles α, β and γ are equal.

Phase	a[Å]	b[Å]	c[Å]	α=β=γ[°]	Volume [Å^3]
Cubic	3.99597	3.99597	3.99597	90	63.8069332
Tetragonal	3.97885	3.97885	4.08358	90	64.6481649
Orthorhombic	3.97178	4.03238	4.04952	90	64.8560878
Rhombohedral	4.01899	4.01899	4.01899	89.833	64.9150326

seems more reliable.

4.2 Strain calculations

4.2.1 (001) oriented crystals

The relative ground state energy for the polar (001)-strained BTO phases are contained in Figure 4.1.

The non-polar centro-symmetric cubic phase is disfavored for all strain values. The phases with polarization axes in the strain plane are more favored for tensile strain, while the phases with polarization normal with the strain plane are more favored at compressive strain. The rhombohedral phase, which has a polarization along the $\langle 111 \rangle$-direction is favored for all strain values. However, we see a gradual shift in the symmetry from a P4mm symmetry at high compressive strain, where the polarization only lies in the direction normal to the strain plane, via a Cm phase at no strain or low tensile strain with polarization in the $\langle 111 \rangle$-direction, to a Amm2 symmetry at high tensile strain, where the polarization direction is contained to the $\langle 011 \rangle$-direction in the strain plane. The tetragonal and orthorhombic out of plane phases relax to the same P4mm symmetry and the same energy level at sufficient compressive strain. In the same manner, the in plane orthorhombic phase becomes symmetry and energy degenerate with

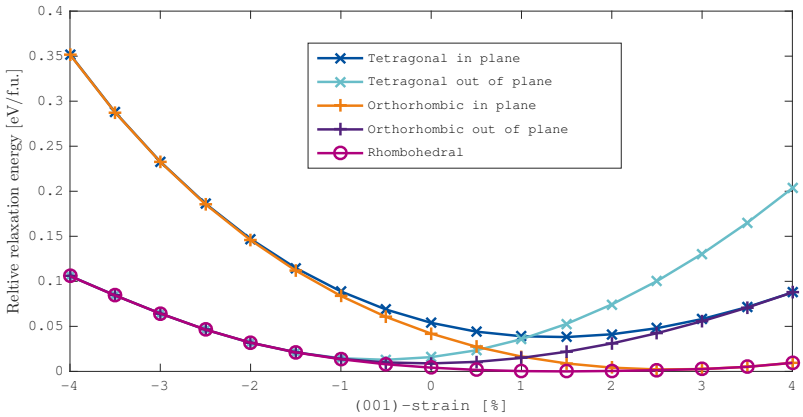

Figure 4.1: The results of the energy relaxations on (001)-oriented strained BTO by initialized unit cell.

the rhombohedral-initialized crystal at sufficient tensile strain. The tetragonal phases show due to their polar axis either polarization fully in the strain plane or fully normal to the strain plane. This limits their ability to switch polarization direction as a function of strain, and they become disfavored as long as the strain is not complimenting their polarization direction. The resulting symmetries of the strain is contained in Figure 4.3.

We find the lowest energy state of the BTO phases at 1.5% tensile strain. As the calculations are normalized to the lattice parameter of the rhombohedral phase as discussed in section 3.3, the mismatch between lattice parameters of the other phases and the rhombohedral will shift the energy curves relative to the mismatch. The rhombohedral phase normally has a unit cell angle of $\alpha = \beta = \gamma = 89.8334°$. This means that the unit cell is elongated along the axis of polarization, the [111] axis. By enforcing cubic strain, the angles are set to 90°, compressing the unit cell in the axis of polarization. The energy curve is shifted towards tensile strain to compensate for the compression.

4.2.2 (111) oriented crystals

As seen in Figure 4.2, there is no phase that is favored for all (111)-strain values. All the calculations done with polar initiation phases become degenerate for large compressive strain values. At 1.5% compressive strain the rhombohedral in plane phase, initialized as the rhombohedral (11-1) phase, find another phase. The tetragonal and orthorhombic phases relax to this phase at 1% tensile strain. The symmetries of the relaxed phases of (111) strained BTO is contained in Figure 4.3.

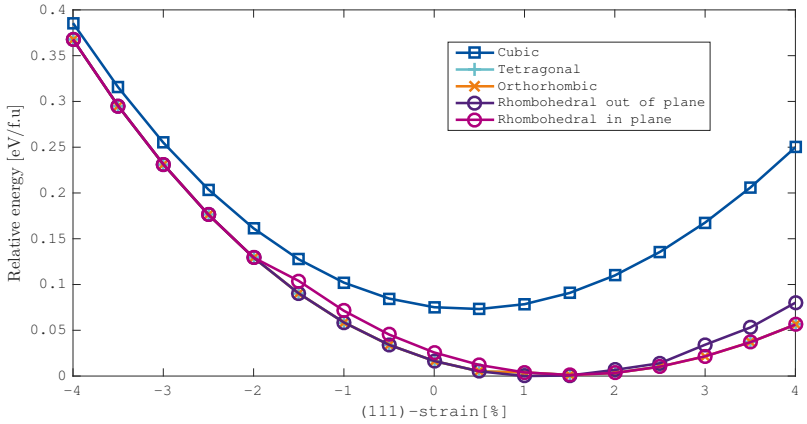

Figure 4.2: The results of the energy relaxations on (111)-oriented strained BTO by initialized phase.

The Cm-symmetric crystal with polarization along the [111]-direction normal to the strain plane is favored for all strain values less than 1.5% tensile strain, where there is a 1st order phase transition to the P1 symmetry. This phase has polarization components both in the strain plane and out of the strain plane.
As for the (001) strained crystals the strain is normalized to the lattice parameter of the rhombohedral phase. The unit cell angles $\alpha = \beta = \gamma = 89.8334°$ are set to 90° to account for cubic strain conditions. The polar axis is therefore compressed just as for the (001) oriented phase. When it's rotated, the strain effects As all the polar phases converge to the same unit cells and energies as the rhombohedral phases for all strain values.

4.2.3 (001) vs (111)

For (001)-strained crystals, the rhombohedral phase is favored for all strain values. However, as sees in Figure 4.3, the symmetry changes as a function of strain. For sufficient compressive strain, the phase has a P4mm- with polarization mainly normal to the strain plane. For tensile strain values larger than 2%, the phase has a Amm2-symmetry, and the polarization is mainly contained in the strain plane along one of the pseudocubic ⟨001⟩ directions. This transition is gradual, as we can see from Figure 4.5. For (111)-strained crystals, there is a 1st order phase transition at 1.5% tensile strain, where the favored state shifts from being a Cm-symmetry, with polarization normal to the strain plane to being a P1-symmetric phase with ion displacement along an axis forming a 19° angle with the strain plane.

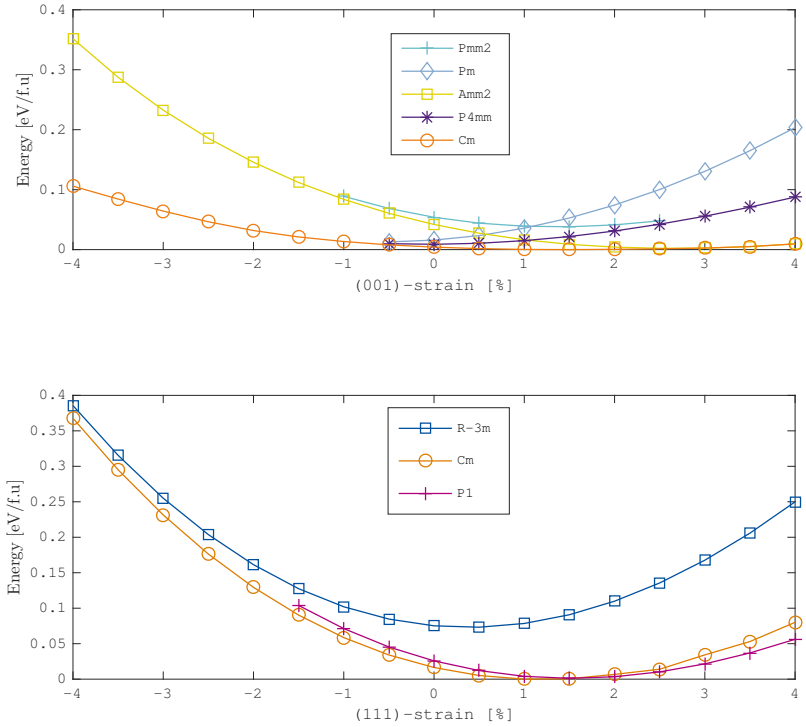

Figure 4.3: Comparison of the relaxation energy of different of symmetries in (001) and (111).

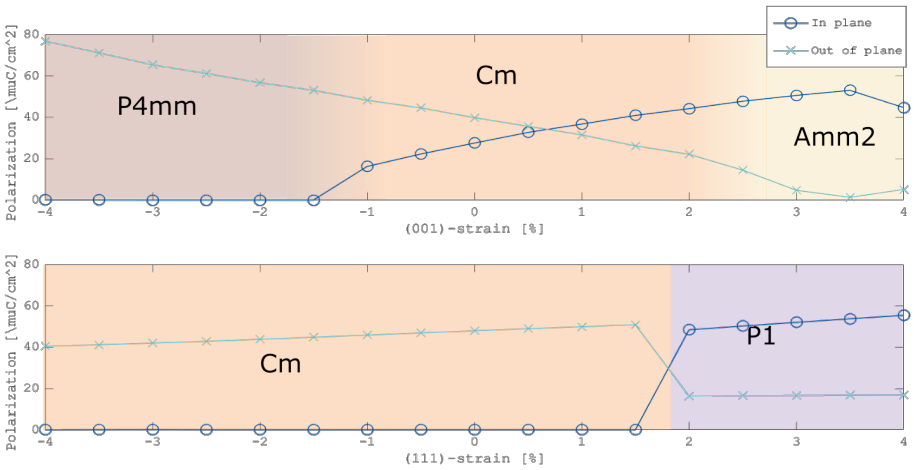

Figure 4.4: Polarization as a function of (001) and (111) strain respectively. (001)-strain induces a gradual phase transition, while (111)-strain leads to 1st order transitions at 1.5% tensile strain.

4.2.4 Polarization

The following section contains the results from the berry phase analysis on the phases of BTO, strained in both (001) and (111) planes. The polarization for the energetically favoured phase for both (001) and (111) strained crystals for each strain value is summed up in Figure 4.4. The detailed Berry phase analysis of the energetically favoured phases are included in this section. The detailed results of the Berry phase calculations on the less favoured phases are found in Appendix B.

Figure 4.5 displays the Berry phase analysis on the rhombohedral (001) strained BTO crystals. Each series consists of the resulting polarization found in structures initialized as a (001)-strained rhombohedral cell, where each data point is a structure distorted between a non-polar reference and the fully relaxed structure in 25% steps, as discussed in section 3.4. The rhombohedrally initialized calculations are favored for all strain values and goes through two 2nd order phase transitions as shown in Figure 4.4. From both figures the gradual transition from polarization completely out of the plane to polarization completely in the plane is apparent.

The rhombohedral phase has a polarization along the $\langle 111 \rangle$ direction, meaning that the Ti^{4+} is displaced towards one of the faces of the oxygen octahedra. For (111)-strained samples, this results in two possible polarizations with respect to the strain plane: one where the polar axis is the [111]-direction and is normal

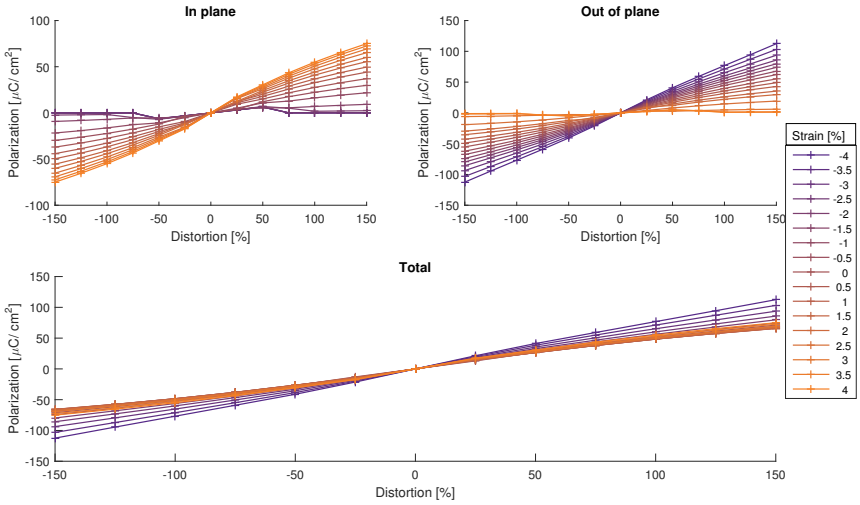

Figure 4.5: Berry phase analysis results from rhombohedral-initialized structures oriented in the (001)-direction. All polarization directions of the rhombohedral phase are symmetry equivalent for (001)-oriented crystals.

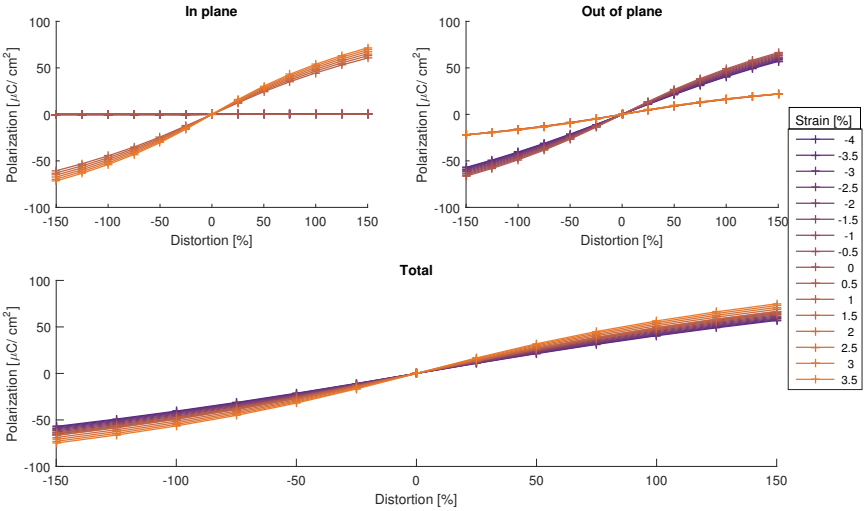

Figure 4.6: Berry phase analysis results from rhombohedral-initialized structures oriented in the (111)-direction, with polarization oriented orthogonal to the strain plane.

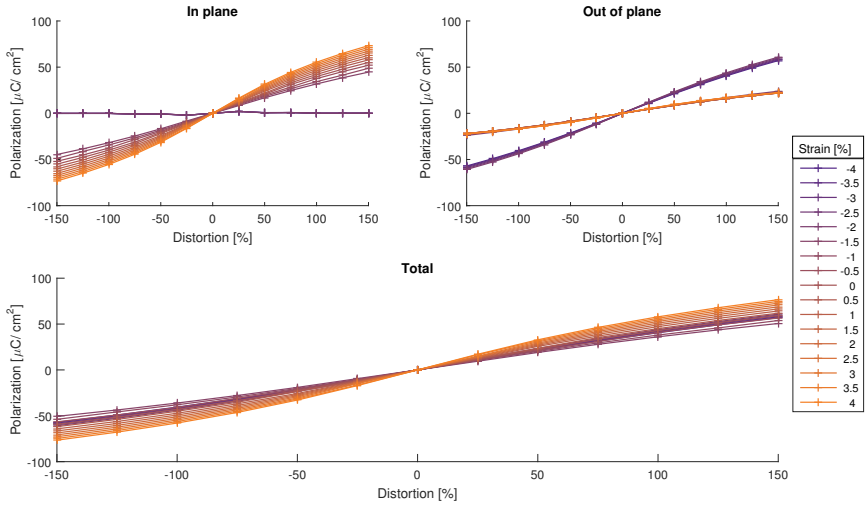

Figure 4.7: Berry phase analysis results from rhombohedral-initialized structures oriented in the (11-1)-direction, with polarization oriented partially in the strain plane.

to the plane, and one where the polarization is the [11-1] direction and forms an approximately 19° angle with the strain plane. Figure 4.6 and Figure 4.7 show the results of the Berry phase analysis on the strained rhombohedral (111) and (11-1) initialized samples respectively. Each series consists of the resulting polarization found in structures initialized as a rhombohedral cell and (111) strained. The phase transition in (111) strained BTO described in Figure 4.4 is between these two phases when the [11-1] phase becomes energetically favored at 2% tensile strain. Strain values lower than 2% tensile strain, the in plane polarization is negligible. For lattice parameters smaller than 2% compressive strain, the two phases relax to the same structure, that are energetically degenerate with equal polarization.

As these are 0 kelvin calculations, the results from the relaxations only give the favorability of the phases at 0 kelvin. The tetragonal phase of BTO is favoured between 5°C and 120°C, so to get an estimate of the polarization as a function of strain at room temperature we might look at the results from the tetragonal phase, summarized in Figure 4.8. When only looking at the tetragonal phase, there is only one phase transition between P4mm and Pmm2. It is a 1st order transition and the polarization flips from being sprightly out of the plane to being sprightly in plane. For (111) the 1st order transition between Cm and P1 symmetries happens earlier than when the rhombohedral phase is allowed.

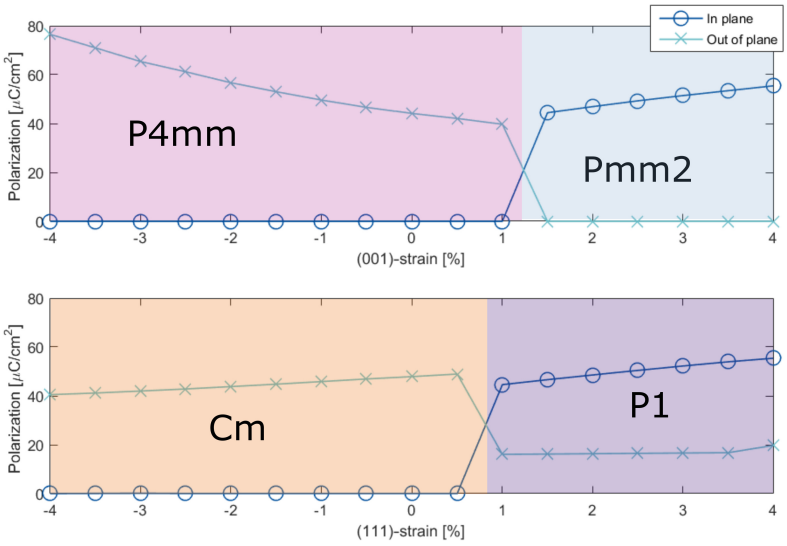

Figure 4.8: Polarization as a function of (001) and (111) strain respectively when only looking at the tetragonal phases.

In Figure 4.9 both the tetragonal and orthorhombic phases are allowed. For (001) the transition to Amm2 is no longer gradual. For (111) the 1st order transition comes for compressive strain. There is also a possibility the polarization drops entirely for compressive strain larger than a certain value. The relative energy difference between the phases decrease as a function of increasing compressive strain, indicating a decrease in coercive energy.

The bulk polarization of BTO is known to be around $26\mu C/cm^2$ [**lines**]. For strained structures, the polarization tends to increase for both compressive and tensile strain. The magnitude of the polarization calculated in these results exceeds this value by a factor of 3-4 in general, however the trends found seem to align with the literature on polarization in BTO.

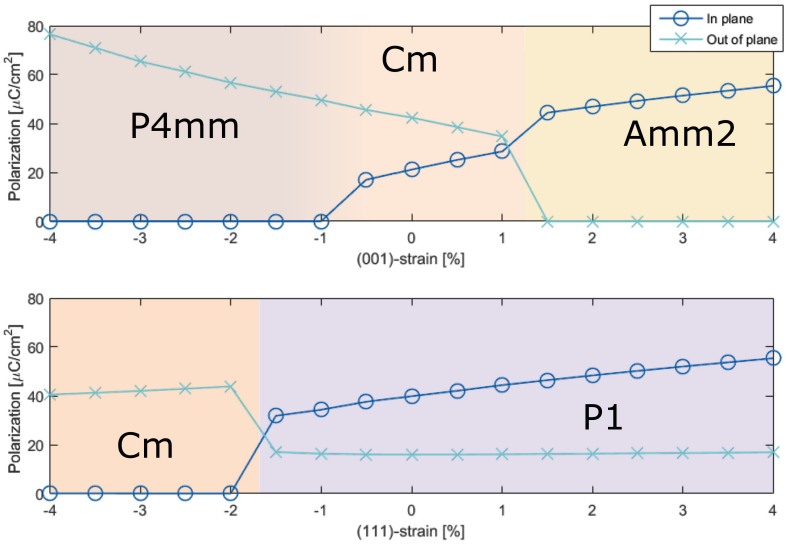

Figure 4.9: Polarization as a function of (001) and (111) strain respectively when only looking at the tetragonal and orthorhombic phases.

Chapter 5

Conclusions

In summary, this thesis has been an exploration into some of the nuances of Density Funtional Theory, ferroelectricity and oxide perovskites, $BaTiO_3$ in particular. The effects of strain and crystal orientation on phase diagram and polarization in BTO has been investigated using DFT calculations and Berry phase analysis. There has been done DFT calculations on bulk BTO as well as epitaxially strained BTO, and by using Berry phase analysis the polarization magnitude and direction of the structures have been estimated. The polarization of (001) strained BTO increase for both compressive and tensile strain as the favoured structure transition from a P4mm symmetry with the extraordinary axis out of the strain plane via a Cm symmetry to a Amm2 symmetry with ion displacements along the pseudocubic [110] direction. For the (111) strained samples the structure has a first order phase transition at 1.5% tensile strain from a Cm symmetry with ion displacements in the out of plane [111] direction to a P1 symmetry. These results are summarized in Figure 4.4. The relative energies are calculated using the PBEsol functional [1, 2]. Polarizations are calculated using Berry phase analysis in VASP.

As the DFT calculations are 0 kelvin calculations, they do not accurately represent the phase diagram at room temperature. To get an estimate of the behaviour at room temperature the tetragonal phase alone is considered, as we know that this is favoured for temperatures between 5°C and 120°C. When considering the tetragonal phase alone, the phase transitions were 1st order for both (001) and (111) strained structures. Further a study of the polarization when both tetragonal and orthorhombic phases are allowed shows the some of the same characteristics as the purely tetragonal results. The magnitude of the polarization found is 3-4 times larger than the $26\mu C/cm^2$ described in literature, however the trends of the polarization as a function of strain is in accordance with the litterature on (001) strained BTO. The work done in this thesis lays the theoretical groundwork

for a polar phase for compressive strain in (111) strained BTO, where all the polar phases converge to a polar out of plane phase for compressive strain. This is contrary to some of the previous work done on (111) oriented BTO stating that BTO relaxes to a non-polar R-3m symmetry for compressive strain values [3, 4]. This study has been conducted using the PBEsol functional [1, 2] as opposed to the LDA functional [5] used in earlier studies. As these results have been shown without considering the effects of domain generation and interface effects, they serve as a first-principle study of the effects of strain and interface orientation on the phases of BTO.

Bibliography

[1] K. Burke J. P. Perdew and M. Ernzerhof. *Generalized gradient approximation made simple*. 1996.

[2] K. Burke J. P. Perdew and M. Ernzerhof. *Erratum: Generalized gradient approximation made simple*. 1997.

[3] Aldo Raeliarijaona and Huaxiang Fu. "Various evidences for the unusual polarization behaviors in epitaxially strained (111) BaTiO3". In: *J. Appl. Phys. 115* (2014).

[4] Riku Oja et al. "Computational study of (111) epitaxially strained ferroelectric perovskites $BaTiO_3$ and $PbTiO_3$". In: *Phys. Rev. B* 78 (9 Sept. 2008), p. 094102. DOI: 10.1103/PhysRevB.78.094102.

[5] J. P. Perdew and A. Zunger. *Self-interaction correction to density-functional approximations for many-electron systems*. 1981.

[6] Emil B Song et al. "Robust bi-stable memory operation in single-layer graphene ferroelectric memory". In: *Applied Physics Letters* 99.4 (2011), p. 042109.

[7] Yasuyuki Hikita Harold Y. Hwang Takeaki Yajima. "A heteroepitaxial perovskite metal-base transistor". In: *Nture Materials* 10 (2011), pp. 198–2010.

[8] V. M. Fridkin. "Ferroelectricity and Giant Bulk Photovoltaic Effect in BaTiO3 Films at the Nanoscale". In: *Ferroelectrics* 484.1 (2015), pp. 1–13. DOI: 10.1080/00150193.2015.1059151. eprint: http://dx.doi.org/10.1080/00150193.2015.1059151.

[9] Alexei Gruverman et al. "Direct studies of domain switching dynamics in thin film ferroelectric capacitors". In: *Applied Physics Letters* 87.8 (2005), p. 082902.

[10] Xiao Wang et al. "Observation of Magnetoelectric Multiferroicity in a Cubic Perovskite System: $LaMn3Cr_4O_12$". In: *Phys. Rev. Lett.* 115 (2015).

[11] Safa Golrokh Bahoosh Steffen Trimper and Julia M. Wesselinowa. "Multiferroic Behavior of BTO-Nanoparticles". In: *Magnetic Particle Imaging: A Novel SPIO Nanoparticle Imaging Technique* 140 (2012), pp. 281–285.

[12] W. Eerenstein et al. "Giant sharp and persistent converse magnetoelectric effects in multiferroic epitaxial heterostructures". In: *Nature Materials* 6 (2007), pp. 348–351.

[13] C. Martin B. Raveau A. Maignan and M. Hervieu. "Colossal Magnetoresistance Manganite Perovskites: Relations between Crystal Chemistry and Properties". In: *Chemistry of Materials* 10.10 (1998), pp. 2641–2652. DOI: 10.1021/cm9801791. eprint: http://dx.doi.org/10.1021/cm9801791.

[14] Matthieu Bugnet et al. "Temperature-dependent high energy-resolution EELS of ferroelectric and paraelectric $BaTiO_3$ phases". In: *Phys. Rev. B* 93 (2 Jan. 2016), p. 020102. DOI: 10.1103/PhysRevB.93.020102.

[15] Ying Wang et al. "Ultrathin Ferroelectric Films: Growth, Characterization, Physics and Applications". In: *Materials* 7 (2014), pp. 6377–6485.

[16] J. J. Peng et al. "Manipulation of orbital occupancy by ferroelectric polarization in LaNiO3/BaTiO3-δ*heterostructures*". In: *Applied Physics Letters* 107 (2015).

[17] M. E. Lines and A. M. Glass. *Principles and Applications of Ferroelectrics and Related Materials*. 1977.

[18] Jiangpeng Chen et al. "Upward ferroelectric self-polarization induced by compressive epitaxial strain in (001) BaTiO3 films". In: *Journal of Applied Physics* 113 (2013).

[19] Jiefang Li et al. "Dramatically enhanced polarization in (001)(001), (101)(101), and (111)(111) BiFeO3BiFeO3 thin films due to epitiaxial-induced transitions". In: *Applied Physical Letters* 84 (2004).

[20] M. M. Duan B. C. Luo D. Y. Wang and S. Li. "Orientation-dependent piezoelectric properties in lead-free epitaxial 0.5BaZr0.2Ti0.8O3-0.5Ba0.7Ca0.3TiO3 thin films". In: *Applied Physics Letters* 103 (2013).

[21] Huaping Wu et al. "Effect of crystal orientation on the phase diagrams, dielectric and piezoelectric properties of epitaxial BaTiO3 thin films". In: *AIP Advances* 6 (2016).

[22] Myung-Geun Han et al. "Ferroelectric Switching Dynamics of Topological Vortex Domains in a Hexagonal Manganite". In: *Advanced Materials* 25.17 (2013), pp. 2415–2421. ISSN: 1521-4095. DOI: 10.1002/adma.201204766.

[23] Nicole A. Benedek and Craig J. Fennie. "Why Are There So Few Perovskite Ferroelectrics?" In: (2013).

[24] Ronald E.Cohen. "Origin of ferroelectricity in perovskite oxides". In: *Nature* 358 (1992), pp. 136–138.

[25] Richard J.D. Tilley. *Understanding Solids (Second Edition)*. 2013.

[26] R. D. King-Smith and David Vanderbilt. "First-principles investigation of ferroelectricity in perovskite compounds". In: *Physical review B* 49.9 (1994).

[27] Zhen Li et al. "Stabilizing Perovskite Structures by Tuning Tolerance Factor: Formation of Formamidinium and Cesium Lead Iodide Solid-State Alloys". In: *Chemistry of Materials* 28.1 (2016), pp. 284–292. DOI: 10.1021/acs.chemmater.5b04107. eprint: http://dx.doi.org/10.1021/acs.chemmater.5b04107.

[28] K. Momma and F. Izumi. "VESTA 3 for three-dimensional visualization of crystal, volumetric and morphology data". In: *J. Appl. Crystallogr.* 44, 1272-1276 (2011).

[29] Wei Cai et al. "Effects of grain size on domain structure and ferroelectric properties of barium zirconate titanate ceramics". In: *Journal of Alloys and Compounds* 480 (2009), pp. 870–873.

[30] Springer Materials. *Springer Materials*. URL: http://materials.springer.com/ (visited on 12/20/2015).

[31] Springer Materials. *BaTiO3, cubic (BaTiO3 ht) Crystal Structure*. 2014. URL: http://materials.springer.com/isp/crystallographic/docs/sd_1801729 (visited on 12/20/2015).

[32] Springer Materials. *BaTiO3 tetragonal (BaTiO3 rt) Crystal Structure*. 2014. URL: http://materials.springer.com/isp/crystallographic/docs/sd_1626717 (visited on 12/20/2015).

[33] Springer Materials. *BaTiO3 orthorhombic (BaTiO3 lt1 orth, T = 235 K) Crystal Structure*. 2014. URL: http://materials.springer.com/isp/crystallographic/docs/sd_1821713 (visited on 12/20/2015).

[34] Springer Materials. *BaTiO3 rhombohedral Crystal structure*. 2014. URL: http://materials.springer.com/isp/crystallographic/docs/sd_1900556 (visited on 12/20/2015).

[35] David Sholl and Janice A Steckel. *DENSITY FUNCTIONAL THEORY - a practical introduction*. 2009.

[36] David J. Griffiths. *Introduction to Quantum Mechanics (Second Edition)*. 2005.

[37] Astrid Marthinsen. *A first-principles Study of epitaxial Interfaces between Graphene and GaAs*. 2014.

[38] Nicola Spaldin. "A beginner's guide to the modern theory of polarization". In: (2012).

[39] M. V. Berry. "Quantal Phase Factors Accompanying Adiabatic Changes". In: *Proceedings of the Royal Society of London A: Mathematical, Physical and Engineering Sciences* 392.1802 (1984), pp. 45–57. ISSN: 0080-4630. DOI: 10.1098/rspa.1984.0023. eprint: http://rspa.royalsocietypublishing.org/content/392/1802/45.full.pdf.

[40] R. Resta. "Theory of the electric polarization in crystals". In: *Ferroelectrics* 136.1 (1992), pp. 51–55. DOI: 10.1080/00150199208016065. eprint: http://dx.doi.org/10.1080/00150199208016065.

[41] G. Kresse and J. Hafner. "Ab initio molecular dynamics for liquid metals". In: *Phys. Rev. B, 47:558* (1993).

[42] G. Kresse and J. Hafner. "Ab initio molecular dynamics simulation of the liquid-metal-amorphous-semiconductor transition in germanium". In: *Phys. Rev. B, 49:14251* (1994).

[43] G. Kresse and J. Furthmüller. "Efficiency of ab-initio total energy calculations for metals and semiconductors using a plane-wave basis set". In: *Comput. Mat. Sci., 6:15* (1996).

[44] G. Kresse and J. Furthmüller. "Efficient iterative schemes for ab initio total-energy calculations using a plane-wave basis set". In: *Phys. Rev. B, 54:11169* (1996).

[45] Sindre Tuset. "Exploration of the Effecs of Strain on the Phases of BaTiO3 Using density Functional Theory". In: *NTNU* (2015).

[46] Martijn Marsman Georg Kresse and Jürgen Furthmüller. *VASP the GUIDE - INCAR*. 2016. URL: `http://cms.mpi.univie.ac.at/vasp/vasp/INCAR_File.html` (visited on 05/20/2016).

Appendix A

Example of input files

A.1 Example of an INCAR file

$system = BaTiO3
PREC = Normal
NELMIN = 4
NELM = 60
EDIFF = 1E-6
EDIFFG = -1E-3
IBRION = 2
ISIF = 3
LREAL = .FALSE.
NSW = 80
ISMEAR = -5
SIGMA = 0.01
ENCUT = 550

ICHARG = 1
ISTART = 1
LWAVE = .FALSE.
LCHARG = .FALSE.

LORBIT = 11

LASPH = .TRUE.

LMAXMIX = 4

NPAR = 4

A.2 Example of KPOINTS-file

```
Automatic mesh
0
Gamma
6 6 6
0 0 0
```

A.3 Example of POSCAR-file

```
New structure
1.00000000000000
3.9171506866909613 0.0000000000000000 0.0000000000000000
0.0000000000000000 3.9171506866909613 0.0000000000000000
0.0000000000000000 -0.0000000000000000 3.9356236092533665
Ba Ti O
1 1 3
Direct
-0.0000000000000000 -0.0000000000000000 0.0049526062869387
0.5000000000000000 0.5000000000000000 0.4964831816930917
0.5000000000000000 0.5000000000000000 0.0167104331358777
0.5000000000000000 0.0000000000000000 0.5133768749420493
0.0000000000000000 0.5000000000000000 0.5133768749420493

0.00000000E+00 0.00000000E+00 0.00000000E+00
0.00000000E+00 0.00000000E+00 0.00000000E+00
0.00000000E+00 0.00000000E+00 0.00000000E+00
0.00000000E+00 0.00000000E+00 0.00000000E+00
0.00000000E+00 0.00000000E+00 0.00000000E+00
```

Appendix B

Graphs of Berry phase calculations for less favoured phases

B.1 (001) Tetragonal in-plane

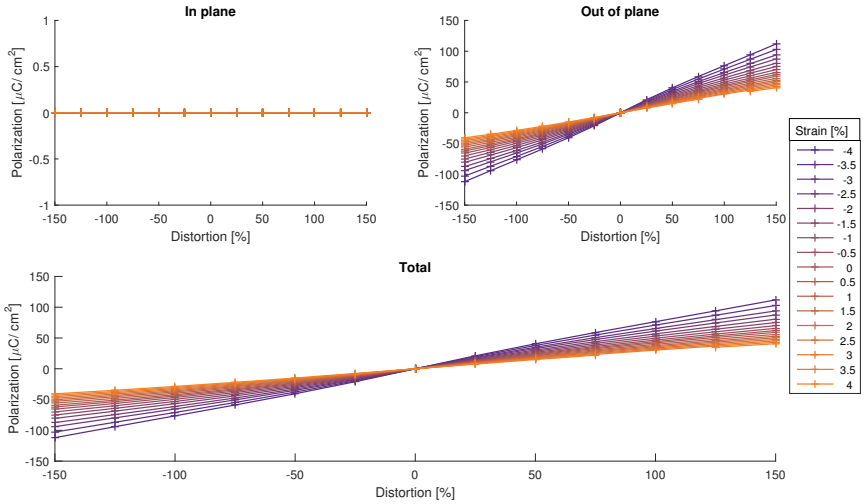

Figure B.1: Berry phase analysis results from tetragonal-initialized structures oriented in the (001)-direction with polarization along the c-axis.

B.2 (001) Tetragonal out of plane

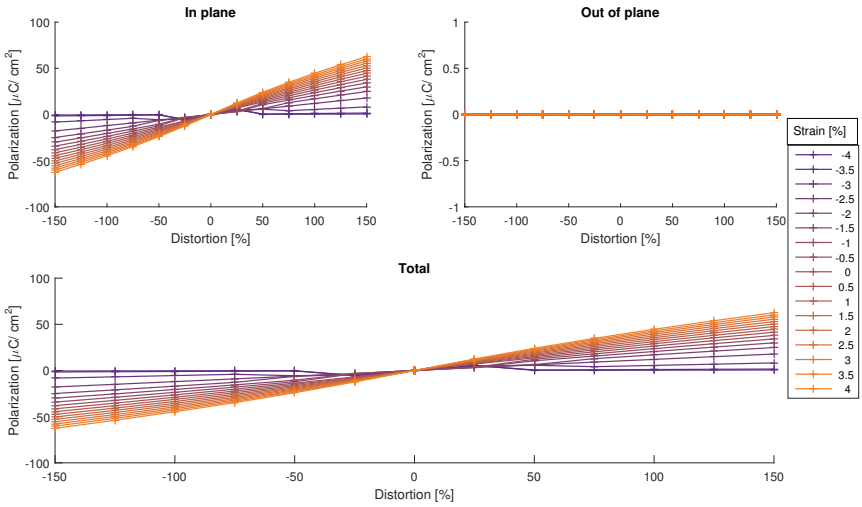

Figure B.2: Berry phase analysis results from tetragonal-initialized structures oriented in the (001)-direction with polarization along the a-axis.

B.3 (001) Orthorhombic out of plane

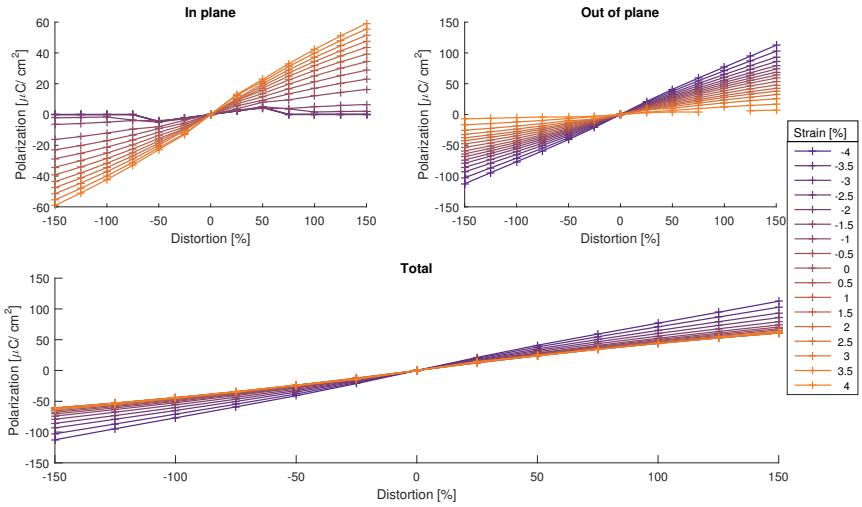

Figure B.3: Berry phase analysis results from orthorhombic-initialized structures oriented in the (001)-direction with polarization in the bc-plane.

B.4 (001) Orthorhombic in-plane

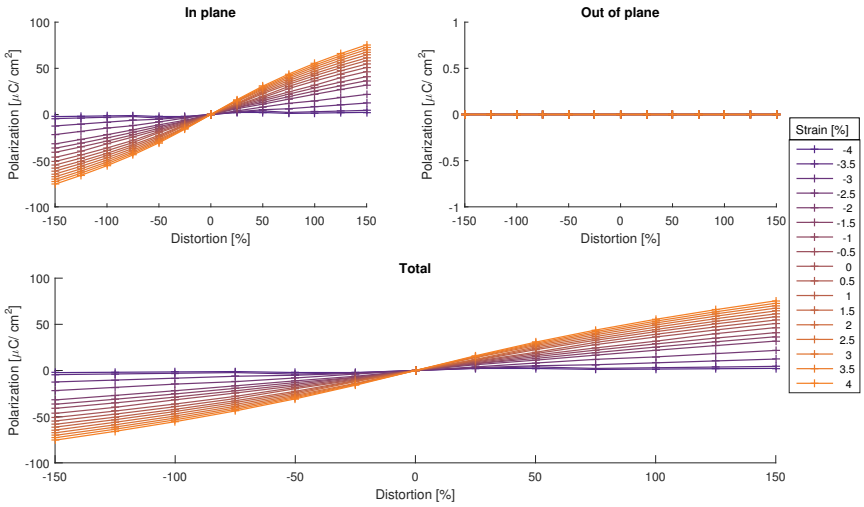

Figure B.4: Berry phase analysis results from orthorhombic-initialized structures oriented in the (001)-direction with polarization along the ab-plane.

B.5 (111) Tetragonal

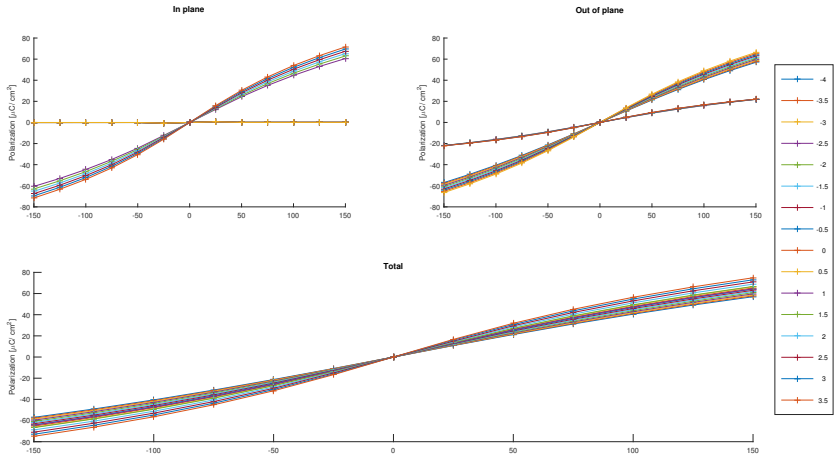

Figure B.5: Berry phase analysis results from tetragonal-initialized structures oriented in the (111)-direction. All polarization directions of the tetragonal phase are symmetry equivalent for (111)-oriented crystals.

B.6 (111) Orthorhombic

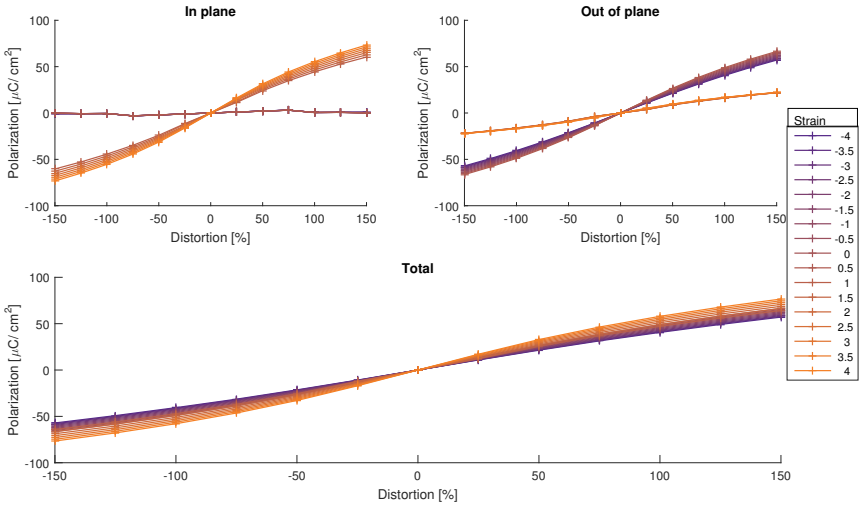

Figure B.6: Berry phase analysis results from orthorhombic-initialized structures oriented in the (111)-direction, with polarization oriented partially out of the strain plane.

Appendix C

Scripts used

C.1 Initstrain

```
a=4.0189879407637594
b=4.0189879407637594
for i in {-8..8}
do
temp=`echo "scale=1; $i/2" | bc -l`
mkdir strain$temp
echo "Initializing strain$temp ..."
cp INCAR POTCAR KPOINTS vaspJob.sh repeatGeomOpt5.sh strain$temp
cp POSCAR POSCARtemp$temp
a_vec=`echo "scale=9;$a*(1+($i/200))" | bc -l`
b_vec=`echo "scale=9;$b*(1+($i/200))" | bc -l`
#sed s/kp/"${K_arr[i]}"/g KPOINTS > K-${K_arr[i]}/KPOINTS
sed -e 's/a_vec/'$a_vec'/g' -e 's/b_vec/'$b_vec'/g' POSCARtemp$temp
 > strain$temp/POSCAR

done
rm POSCARtemp*
echo "Queueing up.."
for dir in strain*; do cd $dir; sbatch vaspJob.sh; cd ..; done
strain_tetragonal/001/ooplane/initstrain.sh (END)
```

C.2 Initialize BP

```
for i in {-150..150..25}
do
mkdir dist$i
echo "Initializing dist$i"
temp=`echo "($i/100)" | bc -l`
./posinterp.pl POSCAR-ref POSCAR-pol $temp
mv POSCAR.out dist$i/POSCAR

cp INCAR KPOINTS POTCAR vaspJob.sh dist$i

done
cp POSCAR-pol dist100/POSCAR
cp POSCAR-ref dist0/POSCAR
echo "Queueing up..."
for dir in dist*; do cd $dir; sbatch vaspJob.sh; cd ..; done
n_rhombohedral/111/11-1/strain-4.0/berryphase/initialize.sh (END)
```

C.3 Posinterpol.pl

```
#!/usr/bin/env perl
#;-*- Perl -*-

# This program interpolates between two POSCAR files by the given f
raction.

use FindBin qw($Bin);
use lib "$Bin";
use lib '/usit/abel/u1/sindretu/Tilleggspakker/vtstscripts-914';
use Vasp;

@args = @ARGV;
@args == 3 || die "usage: posinterp.pl <POSCAR 1> <POSCAR 2> <fract
ional distance between>\n";

$poscarfile1 = $args[0];
$poscarfile2 = $args[1];
$fraction = $args[2];

($coordinates1,$basis,$lattice,$num_atoms,$total_atoms,$selectivefl
ag,$selective)
  =read_poscar($poscarfile1);

print "Read $poscarfile1...\n";

($coordinates2,$basis,$lattice,$num_atoms,$total_atoms,$selectivefl
ag,$selective)
  =read_poscar($poscarfile2);

$description =`head -n 1 $poscarfile1`;
chop($description);

print "Read $poscarfile2...\n";
print "Total atoms: $total_atoms...\n";
print "Lattice: $lattice...\n";

for ($i=0; $i<$total_atoms; $i++) {
    for ($j=0; $j<3; $j++) {
        $interpolated->[$i][$j] = pbc($coordinates1->[$i][$j]+$frac
tion*
        pbc($coordinates2->[$i][$j]-$coordinates1->[$i][$j]));
    }
}

write_poscar($interpolated,$basis,$lattice,$num_atoms,$total_atoms,
$selectiveflag,$selective,$description,"POSCAR.out");

(END)
```